



CHORUS

This is the accepted manuscript made available via CHORUS. The article has been published as:

Wake meandering of a model wind turbine operating in two different regimes

Daniel Foti, Xiaolei Yang, Filippo Campagnolo, David Maniaci, and Fotis Sotiropoulos

Phys. Rev. Fluids **3**, 054607 — Published 22 May 2018

DOI: [10.1103/PhysRevFluids.3.054607](https://doi.org/10.1103/PhysRevFluids.3.054607)

On the wake meandering of a model wind turbine operating in two different regimes

Daniel Foti

*Department of Mechanical Engineering, St. Anthony Falls Laboratory,
University of Minnesota, Minneapolis, Minnesota 55455, USA*

Xiaolei Yang

*Department of Civil Engineering, Department of Mechanical Engineering,
College of Engineering and Applied Sciences, Stony Brook University, Stony Brook, New York 11794, USA*

Filippo Campagnolo

Wind Energy Institute, Technische Universität München, Garching bei München, Germany

David Maniaci

Sandia National Laboratories, Albuquerque, New Mexico 87185, USA

Fotis Sotiropoulos

*Department of Civil Engineering, College of Engineering and Applied Sciences,
Stony Brook University, Stony Brook, New York 11794, USA*

The flow behind a model wind turbine under two different turbine operating regimes (Region 2 for turbine operating at optimal condition with the maximum power coefficient and 1.4 degree pitch angle, and Region 3 for turbine operating at sub-optimal condition with a lower power coefficient and 7 degree pitch angle) is investigated using wind tunnel experiments and numerical experiments using large-eddy simulation (LES) with actuator surface models for turbine blades and nacelle. Measurements from the model wind turbine experiment reveal that the power coefficient and turbine wake are affected by the operating regime. Simulations with and without a nacelle model are carried out for each operating condition to study the influence of the operating regime and nacelle on the formation of the hub vortex and wake meandering. Statistics and energy spectra of the simulated wakes are in good agreement with the measurements. For simulations with a nacelle model, the mean flow field is composed of an outer wake, caused by energy extraction by turbine blades, and an inner wake directly behind the nacelle, while for the simulations without a nacelle model, the central region of the wake is occupied by a jet. The simulations with the nacelle model reveal an unstable helical hub vortex expanding outwards towards the outer wake; while the simulations without a nacelle model show a stable and columnar hub vortex. Because of the different interactions of the inner region of the wake with the outer region of the wake, a region with higher turbulence intensity is observed in the tip shear layer for the simulation with a nacelle model. The hub vortex for the turbine operating in Region 3 remains in a tight helical spiral and intercepts the outer wake a few diameters further downstream than for the turbine operating in Region 2. Wake meandering, a low frequency large-scale motion of the wake, commences in the region of high turbulence intensity for all simulations with and without a nacelle model indicating that neither a nacelle model nor an unstable hub vortex is a necessary requirement for the existence of wake meandering. However, further analysis of the wake meandering and instantaneous flow field using a filtering technique and dynamic mode decomposition show that the unstable hub vortex energizes the wake meandering. The turbine operating regime affects the shape and expansion of the hub vortex altering the location of the onset of the wake meandering and wake meander oscillating intensity. Most importantly, the unstable hub vortex promotes a high amplitude energetic meandering which cannot be predicted without a nacelle model.

I. INTRODUCTION

Average power losses due to the turbine wake in wind farms are reported around 20% [1], however, in some cases can be as high as 80% [2]. In order to optimize wind turbine power production and controls, dynamics of wind turbine wakes must be better understood. Both the velocity deficit and turbulence intensity of the turbine wake are significantly affected by a low frequency large-scale coherent oscillation, the so-called wake meandering. However, the wake meandering mechanism is still far from fully understood [3–5], and low-order models [6, 7] cannot take into account the wake meandering effects accurately. In this study, we attempt to elucidate the details on the dynamics of turbine wake meandering for different turbine operating conditions and assess the corresponding nacelle effects.

Directly behind the turbine a system of helical vortices dominates the flow. As first proposed by Joukowski [8] for a N -bladed propeller, the wake consists of N helical tip vortices, each with circulation Γ , shed from the tip of each turbine blade and an $N\Gamma$ single counter rotating hub vortex oriented along centerline in the streamwise direction. Tip vortices have been characterized by several experimental techniques ([9–12]) and numerical studies ([13–15]). These studies showed that the tip vortices convect downstream due to the relatively high speed flow near the blade tip and eventually breakdown, a process which depends on many factors, such as the turbulence in the incoming flow, rotational speed, geometry of the turbine blade and the interactions of helical vortices. Felli *et al.* [16] observed helical vortex instability modes for a propeller in a water tunnel, while Sarmast *et al.* [17] showed the prevalence of the mutual induction helical instability mode in tip vortices using mode decomposition on tip vortices obtained from a numerical simulation. Recently, Yang *et al.* [18] employed large-eddy simulation (LES) in conjunction with large-scale snow particle image velocimetry (PIV) experiments to investigate the complexity of the coherent structures in the tip shear layer of a utility-scale turbine and uncovered a new instability mode of the tip vortices.

The hub vortex has been studied less extensively than the tip vortices. Okulov and Sørensen [19] performed theoretical stability analysis and concluded that the system of tip vortices and a hub vortex is unconditionally unstable. Felli *et al.* [16] visualized the hub vortex and witnessed its breakdown with relation to the tip vortices. Iungo *et al.* [20] and Viola *et al.* [21] used linear stability analysis on a model turbine and showed that the hub vortex is also unstable. Using geometry-resolving LES with the curvilinear immersed boundary method Kang *et al.* [4] and Foti *et al.* [22] showed that the helical hub vortex forms behind the nacelle and expands in an inner wake (a strong wake at the centerline of the turbine wake) formed by the nacelle for a hydrokinetic turbine and model wind turbine, respectfully. The inner wake recovers and expands quickly allowing the hub vortex to interact with the outer wake (the wake formed by the rotor blades). The interaction of the hub vortex with the outer wake augments the intensity of wake meandering at far wake locations.

Wake meandering, the large scale oscillation of the far wake directly downwind of the breakup of the tip and hub vortices, was observed in experimental measurements and attributed to bluff-body vortex shedding [23, 24]. Several studies [3, 25, 26] observed the low frequency wake oscillations with a similar value of the Strouhal number, the non-dimensional frequency normalized by the rotor diameter and incoming velocity at hub height for various turbines with different operating conditions. However, the effects of the nacelle and operating conditions on wake meandering are still not fully understood and few experiments have been designed for utility-scale turbines to address these issues in particular. While there are several wind tunnel experiments investigating turbine wakes under different operating conditions, such as experiments of the “Blind Test” turbine of diameter 0.9 m and optimal tip speed ratio 6 at Norwegian University of Science and Technology [27–30], and experiments of the MEXICO (Model Experiments in Controlled Conditions) turbine of rotor diameter 4.5 m and optimal tip speed ratio 6.7 at the German-Dutch wind tunnel [31, 32], none of the above experiments addressed the influence of turbine operating conditions on wake meandering.

Numerical investigations, especially using LES, have been used recently to investigate the turbine wake and wake meandering. Due to the high spatial resolution requirement for the geometry-resolving simulations, as found in Kang *et al.* [4] and Foti *et al.* [22], actuator-based turbine models such as the actuator disk [7, 33–35] that models the rotor as a porous disk, the actuator line [14, 36, 37] that models the blades as rotating lines with distributed lift and drag forces, and the actuator surface [38] that distributes the forces over the airfoil surface are commonly employed. Previous numerical (e.g. Yang *et al.* [37]) and experimental (e.g. España *et al.* [39]) results showed that both actuator disk models and actuator line models are able to produce large-scale motion of the wake consistent with wake meandering. However, actuator-based models without accounting for the influence of the nacelle may not be able to capture the hub vortex expansion and its interaction with the outer wake and thus cannot accurately describe the effects of nacelle on the dynamics of wake meandering. Kang *et al.* [4] simulated the flow past a hydrokinetic turbine using three different methods, i.e., the immersed curvilinear boundary method resolving the turbine blades and nacelle and actuator disk/line model with a nacelle model. The study found that the hub vortex from the actuator-based models remains columnar without significant interaction with the outer wake resulting in significantly less turbulence kinetic energy in the far wake. To account for the nacelle effects recent studies included the nacelle geometry to investigate their role in wake dynamics [40–44]. Furthermore, in a recent work by Yang and Sotiropoulos [45], a new

class of actuator surface models for turbine blades and nacelle was developed and validated with the hydrokinetic turbine [4] and MEXICO turbine cases with overall good agreement. The new actuator models for turbine blades and nacelle provided a computationally efficient approach to investigate the similarity in wake meandering statistics from laboratory-scale to utility-scale wind turbines [5].

In this work, we employ both wind tunnel experiments and LES with the new class of actuator surface models developed by Yang and Sotiropoulos [45] to investigate: i) the influence of turbine operating conditions; and ii) the effects of the nacelle on wake meandering of a model turbine. The effects of turbine operating condition on wake meandering were studied for a model turbine [26], atmospheric boundary layer stability [46], and linear stability analysis [42]. The model turbine utilized herein for wind tunnel experiments is intricately designed such that individual blades can be pitched similar to variable speed utility-scale turbines which employ blade pitching to control power output based on the operating conditions. Like utility-scale turbines, the model wind turbine exhibits three main turbine operating regions [47]. Region 1 is a low wind speed regime when the turbine is not run. In Region 2, the turbine operates at its optimal condition with maximum power coefficient and blade pitch angle of 1 degree; while in Region 3, the turbine operates with a relatively low power coefficient and a relatively high blade pitch angle of 7 degrees. To investigate the energetic coherent structures of wake meandering, the meander filtering technique proposed by Howard *et al.* [26], and applied by Foti *et al.* [22] and dynamic mode decomposition [48] are employed to analyze the time series of the computed three-dimensional flow fields.

This paper is organized beginning with section II, a brief summary of the wind turbine design and experimental setup which provide motivation and validation for simulations. The numerical methods of the LES and turbine modeling in section III. Section IV details of the selected test cases and computational setup. The results and analysis are shown in section V. Finally, we have discussions of our results and our conclusion in section VI.

II. EXPERIMENTAL SETUP

Wind tunnel experiments and numerical simulations play a key role in wind turbine design, performance, and optimization. While the wind tunnel experiments cannot reproduce the utility-scale conditions, they can provide key insights and ensure that numerical simulations are reliable through proper validation. The present experiments are designed to acquire measurements of the velocity flow field statistics and energy spectra in the wake of the turbine, turbine power output, and a robust description of realistic wind turbine model and wind tunnel environment that allow us to validate numerical simulations of the model turbine in different operating regimes. Below we detail the wind tunnel experiments and wind turbine model. The experimental measurements of the wake velocity indicate clearly that the turbine power output is a function of blade pitch and tip speed ratio which allow us to delineate turbine operating regimes.

Testing was performed in the closed-return wind tunnel of the Politecnico di Milano (see Campagnolo [49] and Campagnolo *et al.* [50]). The test section, with cross sectional area is $13.84 \text{ m} \times 3.84 \text{ m}$ with a length of 36 m, can generate wind speeds up to 14 m/sec by means of 14 fans, each one consuming up to 100 KW.

This tunnel size allows for the testing of relatively large models with low blockage effects, while atmospheric boundary layer (ABL) conditions can be simulated by the use of turbulence generators such as spires placed at the chamber inlet. A turntable, whose diameter is 13 m, allows for the complete experimental setup to be yawed with respect to the wind tunnel axis, in order to simulate the effect of wind direction changes on the entire setup.

II.1. Wind turbine model: general layout

Tests were conducted with a scaled wind turbine model with a diameter $D = 1.1 \text{ m}$ and height $H = 0.8 \text{ m}$, in the following named **G1** (for Generic wind turbine, 1 m diameter rotor) [50]. The model was designed to satisfy several specific design requirements: i.) a realistic energy conversion process, which means reasonable aerodynamic loads and damping when compared to those of utility-scale wind turbines, as well as wakes of realistic geometry, velocity deficit and turbulence intensity, ii.) collective blade pitch and torque control, as well as yaw setting realized by properly misaligning the tower base with respect to the wind tunnel axis, in order to enable the testing of control strategies, and iii.) a sufficient onboard sensorization, including measures of rotor azimuth, main shaft torque, rotor speed and tower base loads with good accuracy.

The **G1**, whose rated rotor speed is equal to 850 rpm (clockwise rotation), is equipped with three blades mounted on the hub with two bearings, in order to limit flapwise or edgewise free-play. The collective pitch angle can be varied by means of three conical spiral pinions fixed at the blade roots, in turn moved by a driving wheel. The latter, mounted on two bearings held by the rotating hub, is connected, by means of a flexible joint, to a Maxon EC-16 60W brushless motor equipped with a GP22C-128:1 precision gearhead and MR-128CPT relative encoder. The motor is housed in the

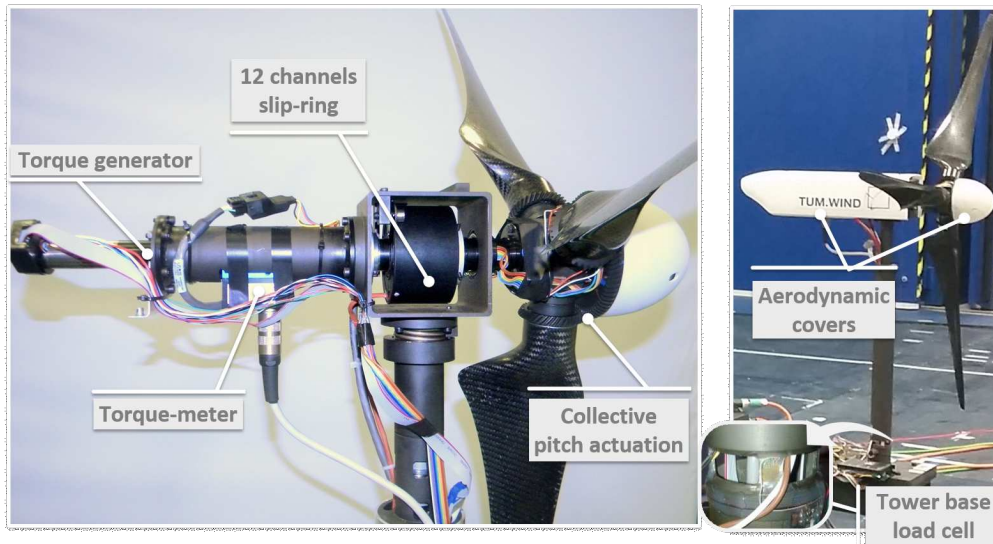


FIG. 1. Overall view of the G1 model, reproduced from Ref. Campagnolo *et al.* [50]. Added for completeness.

hollow shaft and is commanded by an electronic control board EPOS2 24/2 DC housed in the hub spinner. Electrical signals from and to the pitch control board are transmitted by a through-bore 12-channels slip ring located within the rectangular carrying box holding the main shaft.

A LORENZ MESSTECHNIK DR2112-R torque sensor 1 Nm 0.2%, located after the two shaft bearings, allows for the measurement of the torque provided by a Maxon EC-4pole22 90W brushless motor equipped with a GP22HP-14:1 precision gearhead and ENC HEDL 5540 500IMP tacho. The motor is located in the rear part of the nacelle and is operated as a generator by using an ESCON 50/5 4-Q servocontroller. An optical encoder, located between the slip ring and the rear shaft bearing, allows for the measurement of the rotor azimuth.

The tower is designed so that the first fore-aft and side-side natural frequencies of the nacelle-tower group are properly placed with respect to the harmonic per-rev excitations. At its base, strain gages are glued to four CNC-machined small bridges, which were properly sized in order to have sufficiently large strains, in turn required to get accurate outputs from the strain gages. Two electronic boards provide for the power supply and adequate conditioning of this custom-made load cell. Calibration of the cell was performed by using dead weights, stressing the tower with fore-aft and side-side bending moments. Finally, a full 2-by-2 sensitivity matrix is obtained by linear regression. Aerodynamic covers of the nacelle and hub ensure a satisfactory quality of the flow in the central rotor area. Fig. 1 highlights the main features of the G1 model.

II.2. Wind turbine model: rotor aerodynamics

Due to the small dimensions of the scaled wind turbine the low-Reynolds Number airfoil RG14 [51], which is designed in order to achieve a constant lift coefficient C_l along the blade span as described in Burton *et al.* [52], is chosen. Blade chord and twist angle are shown in Fig. 2. The performance of the G1 rotor is measured for different values of the airfoil Reynolds numbers and at several combinations of tip speed ratios (TSR) λ and collective pitch settings β . Significant differences are noticed between the measured and theoretical Blade Element Momentum (BEM)-based aerodynamic performance computed using nominal polars and corrected with an identification procedure [53] used to calibrate the polars leading to a satisfactory agreement as shown in Fig. 3.

II.3. Wind turbine model: control algorithms

The G1 model is controlled by a M1 Bachmann hard-real-time module. Similarly to utility-scale wind turbines, collective pitch-torque control laws are implemented and executed in real-time by the control hardware. Sensor readings are used online to properly compute the desired pitch and torque demands, which are in turn sent to the actuator control boards via analog or digital communication.

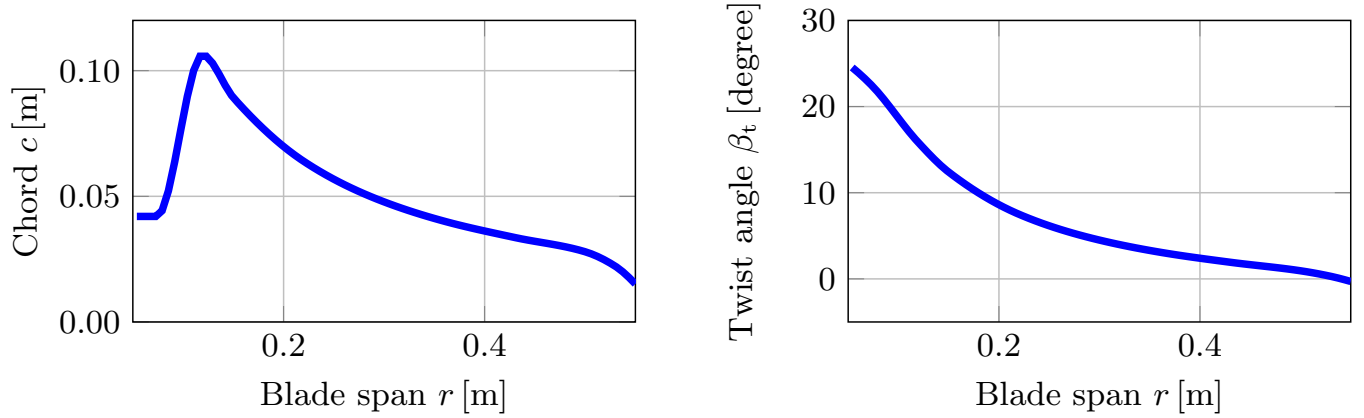


FIG. 2. Blade chord and twist angle.

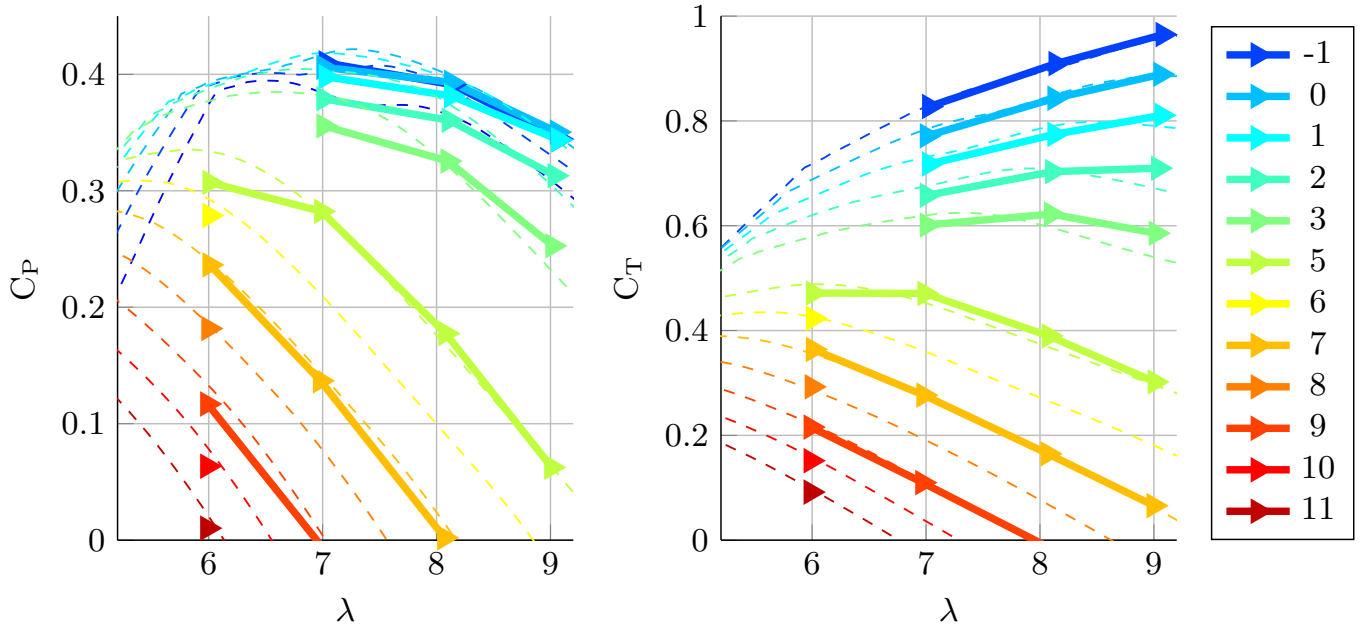


FIG. 3. G1 power (left) and thrust (right) experimental (solid lines) and BEM (dashed lines) coefficients, as function of TSR and blade pitch. The line color indicates the blade pitch in degrees.

Power control is based on the standard wind turbine control structure with two distinct regions, as described in Bossanyi [54]. At low wind speeds, when the wind turbine is operating in the Region 2, the main objective is the maximization of wind turbine power output. This is achieved by keeping the rotor blade pitch angle at a constant value, while the aerodynamic torque reference follows a quadratic function of rotor speed. On the other hand, in high winds, when the wind turbine is operating in the Region 3, generator torque is kept at a constant value (defined by the power reference), while a Proportional Integral Derivative (PID) pitch controller is used to track the rotor speed reference. Transition between two different operating regions is achieved by a control logic that prevents pitch activity at low wind speeds and torque activity at high wind speeds.

The friction acting on the main shaft and due to the bearings and the slip ring brushes is measured before testing, in order to have a reliable measurement of the aerodynamic power. This is obtained by rotating the sole rotor hub, i.e. without blades installed, at several speeds, from rated down to null in steps of 50 rpm. The average measured generator torque is then stored in look-up tables as a function of rotor speed, and it is added during operation in real time to the generator torque reference, in order to allow for the tracking of the aerodynamic torque reference.

III. NUMERICAL METHODS

For the present numerical simulations, we employ LES to solve the three-dimensional, filtered continuity and momentum equations in generalized curvilinear coordinates [55] with a hybrid staggered/non-staggered grid formulation [56]. The governing equations are discretized with three-point central finite differencing and integrated in time using an efficient fractional step method. In compact tensor notation (repeated indices imply summation) the continuity and momentum equations are as follows ($i, j = 1, 2, 3$):

$$J \frac{\partial U^i}{\partial \xi^i} = 0, \quad (1)$$

$$\frac{1}{J} \frac{\partial U^i}{\partial t} = \frac{\xi_l^i}{J} \left(-\frac{\partial}{\partial \xi^j} (U^j u_l) + \frac{\mu}{\rho} \frac{\partial}{\partial \xi^j} \left(\frac{g^{jk}}{J} \frac{\partial u_l}{\partial \xi^k} \right) - \frac{1}{\rho} \frac{\partial}{\partial \xi^j} \left(\frac{\xi_l^j p}{J} \right) - \frac{1}{\rho} \frac{\partial \tau_{lj}}{\partial \xi^j} + F_l \right), \quad (2)$$

where $\xi_l^i = \partial \xi^i / \partial x_l$ are the transformation metrics, J is the Jacobian of the geometric transformation, u_i is the i th component of the velocity vector in Cartesian coordinates, $U^i = (\xi_m^i / J) u_m$ is the contravariant volume flux, $g^{jk} = \xi_l^j \xi_l^k$ are the components of the contravariant metric tensor, ρ is the density, μ is the dynamic viscosity, p is the pressure, and τ_{ij} represents the anisotropic part of the subgrid-scale stress tensor. A body force F_l is used to account for the forces exerted by the actuator-based model. A dynamic Smagorinsky model [57] developed by Germano *et al.* [58] is used for closure of τ_{ij} :

$$\tau_{ij} - \frac{1}{3} \tau_{kk} \delta_{ij} = -2\mu_t \tilde{S}_{ij}, \quad (3)$$

where the $\tilde{(\cdot)}$ denotes the grid filtering operation, and \tilde{S}_{ij} is the filtered strain-rate tensor. The eddy viscosity μ_t is given by

$$\mu_t = \rho C_s \Delta^2 |\tilde{S}|, \quad (4)$$

where C_s is the dynamically calculated Smagorinsky constant [58], Δ is the filter size taken as the cubic root of the cell volume, and $|\tilde{S}| = (2\tilde{S}_{ij} \tilde{S}_{ij})^{\frac{1}{2}}$. In computing C_s , contraction of the Germano identity is carried out using the formulation for general curvilinear coordinates presented in Armenio and Piomelli [59]. A local averaging is then performed for the calculation of C_s since there are no homogeneous directions in the present cases.

III.1. Actuator surface model for turbine blades and nacelle

In the actuator surface model for the blade, the blade geometry is represented by a surface formed by the chord lines at every radial location of the blade. The forces are calculated in the same way as in the actuator line model using the blade element approach. The lift (\mathbf{L}) and drag (\mathbf{D}) at each radial location are calculated as follows:

$$\mathbf{L} = \frac{1}{2} \rho C_L c |\mathbf{V}_{rel}|^2 \mathbf{n}_L, \quad (5)$$

and

$$\mathbf{D} = \frac{1}{2} \rho C_D c |\mathbf{V}_{rel}|^2 \mathbf{n}_D, \quad (6)$$

where C_L and C_D are the lift and drag coefficients from a look-up table created from aerodynamic data for the RG14 airfoil obtain using XFOIL [60], c is the chord, \mathbf{V}_{rel} is the relative incoming velocity, and \mathbf{n}_L and \mathbf{n}_D are the unit vectors in the directions of lift and drag, respectively. The relative incoming velocity \mathbf{V}_{rel} is computed by

$$\mathbf{V}_{rel}(\mathbf{X}_{LE}) = u_x(\mathbf{X}_{LE}) \mathbf{e}_x + (u_\theta(\mathbf{X}_{LE}) - \Omega r) \mathbf{e}_\theta, \quad (7)$$

where \mathbf{X}_{LE} represents the leading edge coordinates of the blade, Ω is the rotational speed of the rotor, \mathbf{e}_x and \mathbf{e}_θ are the unit vectors in the axial flow and rotor rotating directions, respectively. In the present model, the axial and azimuthal components of the flow velocity, i.e. u_x and u_θ are computed at the leading edge of the blade. Generally, the leading edge point LE does not coincide with any background nodes. In the present work, the smoothed discrete

Region	β [deg]	Tip-speed ratio	C_p	C_T	$Re_D = U_{hub}D/\nu$
2	1.4	8.1	0.45	0.79	4.4×10^5
3	7.0	8.1	0.25	0.3	5.1×10^5

TABLE I. Turbine operating condition parameters and performance.

delta function (i.e. the smoothed four-point cosine function) proposed by Yang *et al.* [61] is employed to interpolate the flow velocity at the leading edge of the blade from the background grid nodes. The forces computed on each grid node of the leading edge are then uniformly distributed onto the corresponding actuator surface meshes with the same radius from the rotor center. The forces on the blade actuator surface are then distributed to the background grid nodes for the flow field using the same discrete delta function employed in the velocity interpolation process. The stall delay model developed by Du and Selig [62] and the tip-loss correction proposed by Shen *et al.* [63] are employed to take into account the three-dimensional effects.

In the actuator surface model for the nacelle, the nacelle geometry is represented by the actual surface of the nacelle with distributed forces. The force on the actuator surface is decomposed into two parts: the normal component and the tangential component. The normal component of the force is computed in a way to satisfy the non-penetration condition, which is similar to the direct forcing immersed boundary method [64] as follows:

$$F_n = \frac{(\tilde{\mathbf{u}}(\mathbf{X}) - \mathbf{u}^d(\mathbf{X})) \cdot \mathbf{n}(\mathbf{X})h}{\Delta t}, \quad (8)$$

where \mathbf{X} represents the coordinates of the nacelle surface mesh, $\mathbf{u}^d(\mathbf{X})$ is the desired velocity on the nacelle surface, $\mathbf{n}(\mathbf{X})$ is the unit vector in the normal direction of the nacelle, $\tilde{\mathbf{u}}$ is the velocity estimated from the previous flow field using an explicit Euler scheme, $h = (h_x h_y h_z)^{1/3}$ (h_x , h_y and h_z are the background grid spacings in the x , y and z directions, respectively), and Δt is the time step. The tangential force is assumed to be proportional to the incoming velocity U and is computed as follows:

$$F_t = \frac{1}{2} c_f U^2, \quad (9)$$

where c_f is calculated from the empirical relation proposed by F. Schultz-Grunow [65]. The direction of the tangential force is determined by the local tangential velocity. The smoothed discrete delta function is employed for the velocity interpolation and force distribution as in the actuator surface model for blades. Validations of the actuator surface models for turbine blades and nacelle can be found in [45].

IV. TEST CASES AND COMPUTATIONAL SETUP

Here, we discuss the computational details and overall setup for the two wind tunnel experiments where measurements of the velocity flow field are taken at two different operating conditions of Region 2 and Region 3 with the corresponding setup shown in Table I.

The wake behind the rotor was traversed and measured using 2 Tri-axial fiber-film probes *Dantec 55R91*, while wind speed was also constantly measured by means of a Pitot tube located 1.5D in front of the rotor disk and at hub height, as shown in Fig. 4. The pressure signals were acquired by a *MENSORCPT-6100 FS.=0.36PSI* Pitot transducer. Campagnolo *et al.* [50] used this setup to investigate yaw misalignment and wind turbine power output, this study will focus on the the acquired data for the mean velocity flow field of the wake and energy spectra along the hub height plane.

Simulations are designed to reproduce the real wind tunnel environment based on the experiments including the spires at the inlet to induce a turbulent boundary layer that resembles an atmospheric boundary layer. A sketch of the entire wind tunnel domain with upstream spires and turbine is shown in Fig. 5(a). A precursor LES of the entire wind tunnel without the turbine but resolving the details of the spire geometry using the curvilinear immersed boundary method is performed to acquire inflow conditions for subsequent turbine simulations [66]. The dimensions of the wind tunnel domain are as follows: spanwise width $L_z/D = 12.5$, height $L_y/D = 3.5$, and a streamwise length $L_x/D = 31.8$. The computational domain is discretized with $600 \times 180 \times 1200$ cells in spanwise, vertical and streamwise directions, respectively. Fourteen spires, resolved using the curvilinear immersed boundary method, with a height $H_s/D = 1.8$ and width $S_s/D = 0.45$ are placed one meter apart symmetrically around the wind tunnel centerline. The trailing edge of the spires is placed at a streamwise distance of 2.3 diameters downstream of the domain inlet. Uniform inflow velocity U_b is applied at the inlet. A wall model for smooth walls [37] is employed on the top, bottom

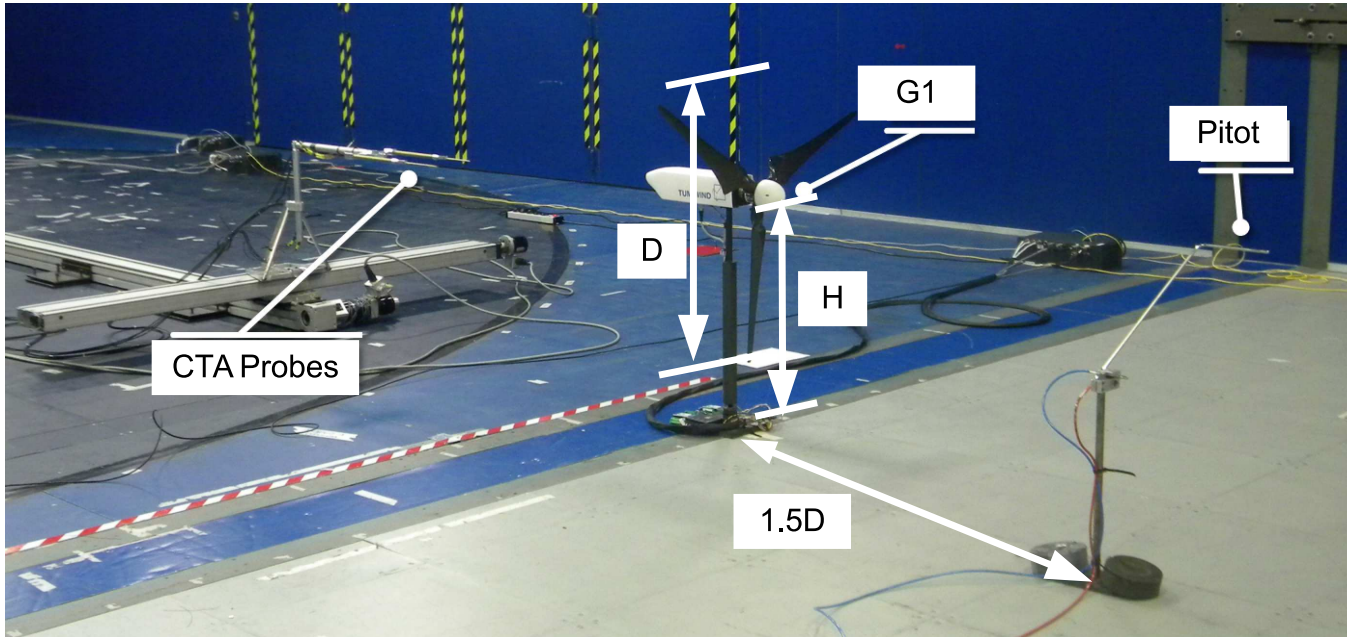


FIG. 4. Experimental setup in the wind tunnel

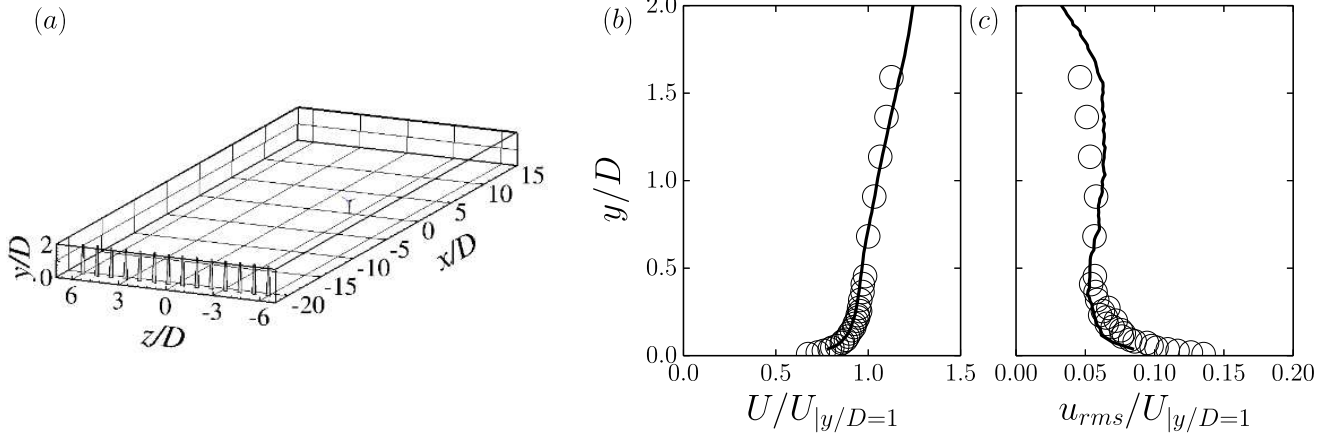


FIG. 5. (a) Sketch of the wind tunnel domain with spires at the inlet ($x/D = -20.5$) and turbine located at ($x/D = 0$ and $z/D = -2.5$). Comparison of the vertical profiles at $x/D = 3.5$ from a precursor simulation (solid lines) with measurements (circles) for an empty wind tunnel for (b) mean streamwise velocity and (c) rms (root-mean-squared) of streamwise velocity fluctuations.

and side walls of the domain, while boundary conditions on the spires are applied on the grid nodes in the vicinity of the spires using wall model reconstruction as described in Kang and Sotiropoulos [67]. Further analysis of the precursor simulation and the generated inflow resemblance to an atmospheric boundary layer can be found in Foti *et al.* [66]. The instantaneous flow field is acquired and saved at the location upstream of the turbine at $x/D = -1.5$, and is fed into the wind turbine simulations.

The mean streamwise velocity and rms (root-mean-square) streamwise velocity from the precursor simulation with the spires without the wind turbine at $x/D = 3.5$ are shown in Fig. 5(b) and Fig. 5(c), respectively, where both the simulations and experimental measurements converge to the same profile. At this location the velocity at turbine hub height is $U_{hub}/U_b = 1.0$, the incoming shear velocity is $u_\tau/U_b = 0.03$, and boundary layer height is $\delta/D = 1.8$, the same as the height of the spires. The Reynolds number based on U_{hub} and D is 4.0×10^5 . The value of Reynolds number of the empty wind tunnel simulations and turbine simulations in both operating conditions are beyond the value for which Reynolds number independence for turbine wakes is observed [68]. The so-generated inflow flow fields

from this precursor simulation are employed to provide inflow conditions in the simulations for both turbine operating conditions without running additional precursor simulations to match the specific values of Reynolds number.

The turbine simulations are performed in a domain $12.5D \times 2.7D \times 16D$ in spanwise, vertical and streamwise directions, respectively. The numbers of grid nodes are $272 \times 120 \times 589$ in spanwise, vertical and streamwise directions, respectively, resulting in a grid spacing $D/50$ in all three directions. This resolution is comparable to other studies using actuator-type models [14, 69] and is sufficient to capture the main characteristics of the turbine wake as shown in Fig. 6 and Fig. 7 where we compare the computed results with experimental measurements. With this domain, the turbine is placed at the same location $x_0/D = 20.5$ downstream of the spires and $z_0/D = -2.5$ as prescribed in the experiments. Similar to the precursor simulations, bottom and side walls of the domain utilize a wall model for smooth walls. Unlike the precursor simulation, the vertical extend of the domain is truncated at $2.7D$ in a region of uniform velocity outside the boundary layer and the top boundary is a free-slip boundary condition. The height of boundary layer, δ_t , on the top of the wind tunnel at the location of the wind turbine is small ($\delta_t/D \approx 0.35$) compared to the height of the boundary layer in which the turbine operates ($\delta/D \approx 1.8$) and is nearly $2D$ from the top-tip of the wind turbine blade. We assume that the top of the wind tunnel has a negligible effect on the wind turbine operation. Two simulations for each turbine operating conditions based on the experimental setup shown in Table I are carried out: one with the actuator surface models for the blades and nacelle (R2-BN and R3-BN for Region 2 and Region 3, respectively); the other one with actuator surface model for the blades only (R2-B and R3-B for Regions 2 and 3, respectively).

V. RESULTS

We present and analyze the computational and experimental results in this section. In section V.1, we first compare the computed profiles with measurements at different downstream locations and show the time-averaged flow field and turbulence statistics for simulations with and without a nacelle model for the two different turbine operating conditions. We then present instantaneous flow fields for different cases and analyze the power spectral density in section V.2, and investigate the wake meandering using a filtering technique and dynamic mode decomposition in section V.3 and section V.4, respectively.

V.1. Time-averaged characteristics

To evaluate the capability of the actuator surface models in predicting the wake from the model wind turbine, we compare the computational results with the experimental measurements for the turbine operating in Region 2 and Region 3 in Fig. 6 and Fig. 7, respectively. Figure 6(a) shows the comparisons of the spanwise profiles of the mean streamwise velocity deficit, $1 - U/U_\infty$, where U_∞ is the mean freestream velocity at the boundary layer height. In the profiles closest to the turbine at $x/D = 1.4$ and $x/D = 1.7$, the effect of the nacelle manifests itself as an increase of the streamwise velocity deficit along the centerline and delineates two distinct wake regions: the inner wake mainly formed by the nacelle, and the outer wake created by the blades. The employed nacelle model captures this inner wake feature from the nacelle, but the absence of a nacelle model results in an unphysical jet at the center of the profiles. On the other hand, the shear layer of the outer wake, mainly caused by the forces on the blades extending to $z/D \pm 0.5$ (along the horizontal dotted lines in Fig. 6) is captured well by both simulations with and without a nacelle model. Further downstream of the rotor, the inner wake of the nacelle begins to merge with the outer wake and the streamwise velocity deficit begins to flatten along the centerline. The unphysical jet in the simulation without the nacelle model begins to dissipate at further downstream locations as the corresponding agreement with experimental measurements becomes better. Far from the rotor $x/D > 4.0$, the wake recovery becomes slow for all the cases. Figure 6(b) shows the comparisons of the mean vertical velocity V which represents the rotational velocity on this plane. Both simulations with and without a nacelle model agree well with the experimental measurements. Close to the turbine, the rotation of the blades imparts a strong mean rotation on the inner wake that peaks just away from the center. Despite the high rotational velocity occurring near the nacelle boundary, the nacelle model does not affect the mean vertical velocity, which is due only to the rotation of the rotor. Farther downstream the mean rotation quickly dissipates. The mean spanwise velocity W is shown in Fig. 6(c). The simulations compare well with the measurements despite the small magnitude of this velocity component. The final experimental measurement for this operating regime, shown in Fig. 6(d), is the streamwise rms (root-mean-square) velocity u' . The cases with and without a nacelle model capture the magnitude of the turbulence intensity of nearly 0.2 within the tip shear layer showing agreement with the experiments. Near the centerline and $x/D = 1.4$, both the measurements and the simulation with a nacelle model capture the shear layer of the inner wake with a slight increase of the turbulence intensity. The simulation without the nacelle model shows an unphysical increase peaking at the centerline. As the

wake progresses downstream, the centerline peak of turbulence intensity in the simulation without a nacelle model decreases and converges to the measurement profiles at $x/D = 3$. Furthermore, as the inner and outer wake shear layer expand, the turbulence intensity along the tip positions relaxes to about $u'/U_\infty = 0.1$ where the measurements and both simulations with and without a nacelle model agree well with each other.

The spanwise profiles of the mean velocity deficit of the measurements and simulations for the turbine operating in Region 3 are shown in Fig. 7(a). In comparison with the turbine operating in Region 2, significantly less velocity deficit is in the region near blade tips at near wake locations ($x/D = 1.4, 1.7, 2$). Near the centerline the velocity deficit is lower and the inner wake of the nacelle is smaller with a flattened profile. Similarly, the simulation without a nacelle model under predicts the velocity along the centerline until $x/D > 2$. Far away from the turbine rotor, the wake relaxes and all of the simulation cases are able to accurately simulate the wake. The comparison of the vertical velocity V profiles (rotational component on this plane) is shown in Fig. 7(b). In comparison with the turbine operating in Region 2, the magnitude of rotational velocity near the blade tips are smaller for the turbine operating in Region 3 at near wake locations ($x/D = 1.4, 1.7, 2$). The spanwise velocity W profiles shown in Fig. 7(c), on the other hand, are similar to the profiles for the turbine operating in Region 2 and both simulations with and without nacelle model show good agreement with the measurements. Finally, the streamwise rms velocity is shown in Fig. 7(d). Similar to what we observed in Fig. 6(d) for the turbine operating in Region 2, the lack of a nacelle model introduce peaks on the streamwise turbulence intensity in the region near the rotor centerline at near wake locations ($x/D = 1.4, 1.7, 2$). The tip shear layer is accurately simulated by all the simulations. As the wake progresses downstream, differences in the mean flow field are not obvious.

Next, we investigate the spatial distribution of the mean flow field via contour plots. Mean flow and turbulence quantities for the Region 2 simulations with and without a nacelle model on the vertical-streamwise centerline plane are shown in Figs. 8(a)-(d) and Figs. 8(e)-(h), respectively. The mean streamwise velocity U/U_{hub} for the simulation with a nacelle model in Fig. 8(a), shows the outer wake formed by the turbine rotor and the inner wake behind the nacelle (outer and inner wake are demarcated on figure). In the mean velocity contour shown in Fig. 8(e) for the simulation without a nacelle model, a jet exists along the centerline, as discussed in the spanwise profile shown in Fig. 6 and Fig. 7 and seen in simulations in Kang *et al.* [4], exists as a consequence of not having the blockage effect of a nacelle body. The outer wake shear layer at the top tip position immediately downstream of the turbine is very sharp and slowly expands. The inner wake forms a core region where the hub vortex begins to grow.

The turbulence kinetic energy k/u_τ^2 (TKE) contours from the simulations with and without a nacelle model are shown in Fig. 8(b) and Fig. 8(f), respectively. As seen, the intense turbulence regions start at the rotor tips. From the TKE of the simulation with a nacelle model, the outer wake and the expanding inner wake are observed. The inner wake expands outwards towards and intercepts the outer wake a few diameters downstream of the turbine. Near this intersection, there is a marked increase in TKE caused by the interaction of the expanding inner wake and the outer wake. The growth of a large region of high TKE in the tip shear commences near the intersection of the inner wake shear layer. In Kang *et al.* [4] and with further evidence in Foti *et al.* [22], this region of high TKE is associated with the onset of wake meandering. For the simulation without a nacelle model, a hub vortex is still formed along the centerline of the turbine but no inner wake is formed. The increase in streamwise velocity causes the hub vortex to remain strong and columnar. Expansion of the hub vortex towards the remnants of the tip vortices at the tip position does not occur. Instead, the onset of wake meandering occurs with less turbulence energy and further downstream. The location of the maximum TKE occurs at $x/D = 3$ for the simulation with a nacelle model; while it is found to be at $x/D = 3.5$ for the simulation without a nacelle model. The locations are shown on the TKE contours in Fig. 8(b) and Fig. 8(f) as large circles.

The mean rotational velocity in the wake is expressed as the mean spanwise velocity W/U_{hub} where positive is the direction into the page. For reference, the turbine rotates clockwise, thus the top blade tip is moving out of the page. In Fig. 8(c) and Fig. 8(g), showing the simulations with and without a nacelle model, respectively, a mean rotational rate is present at turbine near wake locations. Both figures show a wake that is rotating counter-clockwise (opposite the rotation of the turbine blades) with the strongest rotation occurring near the root of the blade. By the tip of the blade, the rotation is nearly zero. By $x/D = 5$, the mean rotation in the wake has dissipated to be negligible.

The streamwise-vertical Reynolds stress $\overline{u'v'}/u_\tau^2$ for simulations with and without a nacelle model, shown in Fig. 8(d) and Fig. 8(h), respectively, shows the turbulence shear stress and mixing that occurs in the shear layers of the inner and outer wake. There are several regions of intense shear stress in the simulation with a nacelle model: i.) The turbine tip shear layer which extends into the wake as a thin layer for the first few diameters downstream where the tip vortices remain coherent occupying the interface between the fast moving outer flow and the turbine wake. As the tip vortices start to breakdown the region of mixing begins to expand through entrainment of fluid from outside the wake; ii.) Behind the nacelle along the shear layer of the inner wake. This region of high Reynolds stress promotes mixing of the slowest moving inner wake with the outer wake behind the turbine blades. Moreover, this allows for entrainment of fluid into the inner wake and rapid expansion of the inner wake and hub vortex. Encompassing the inner wake is a region of opposite-sign low Reynolds shear stress that originates from the root of the turbine blades;

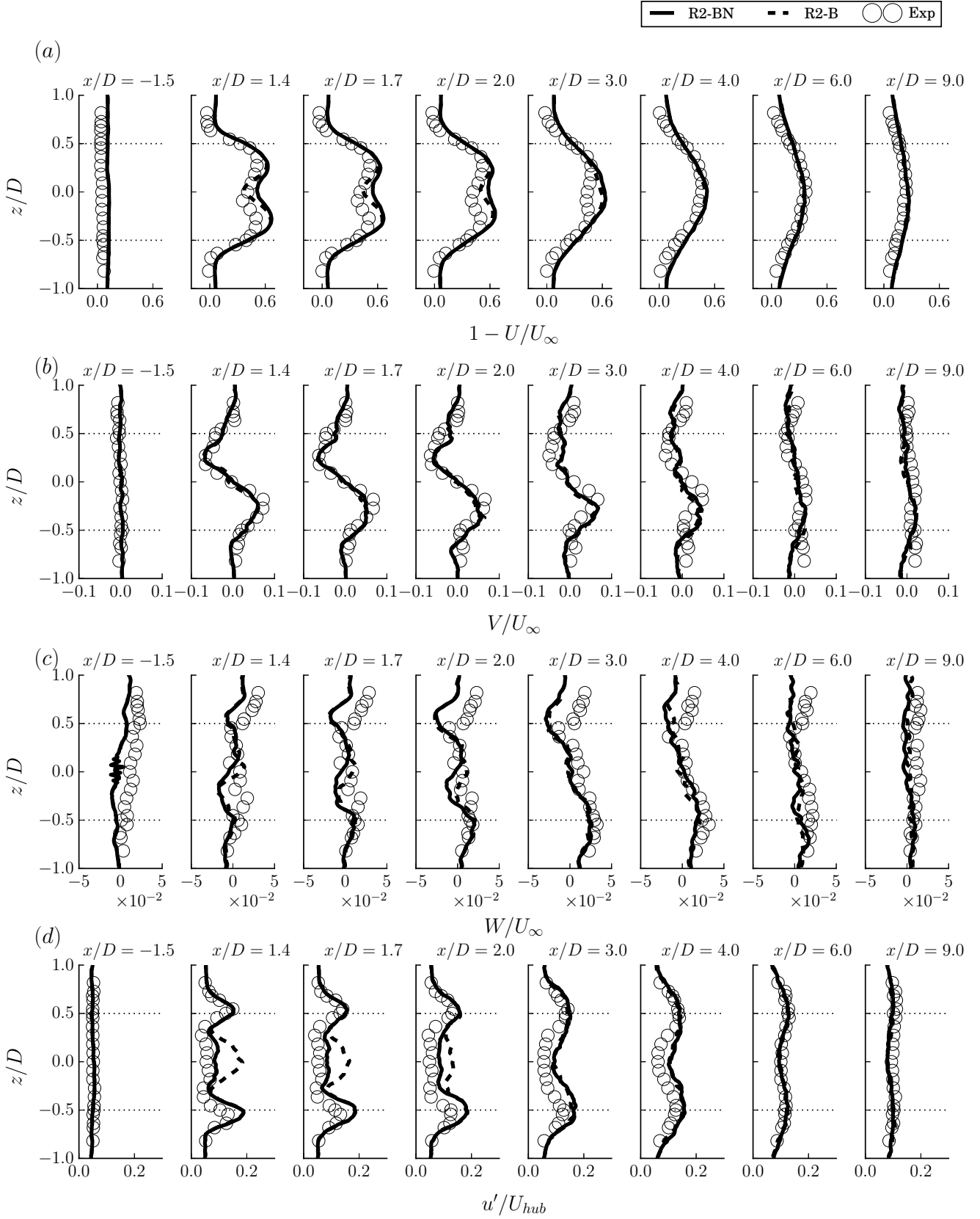


FIG. 6. Comparisons of the computed and measured spanwise profiles for the Region 2 case for (a) streamwise velocity deficit, (b) vertical velocity, (c) spanwise velocity, and (d) streamwise RMS velocity u' . The horizontal dotted lines at $z/D = \pm 0.5$ are the tip positions. The velocity is non-dimensionalized by U_∞ , the mean freestream velocity.

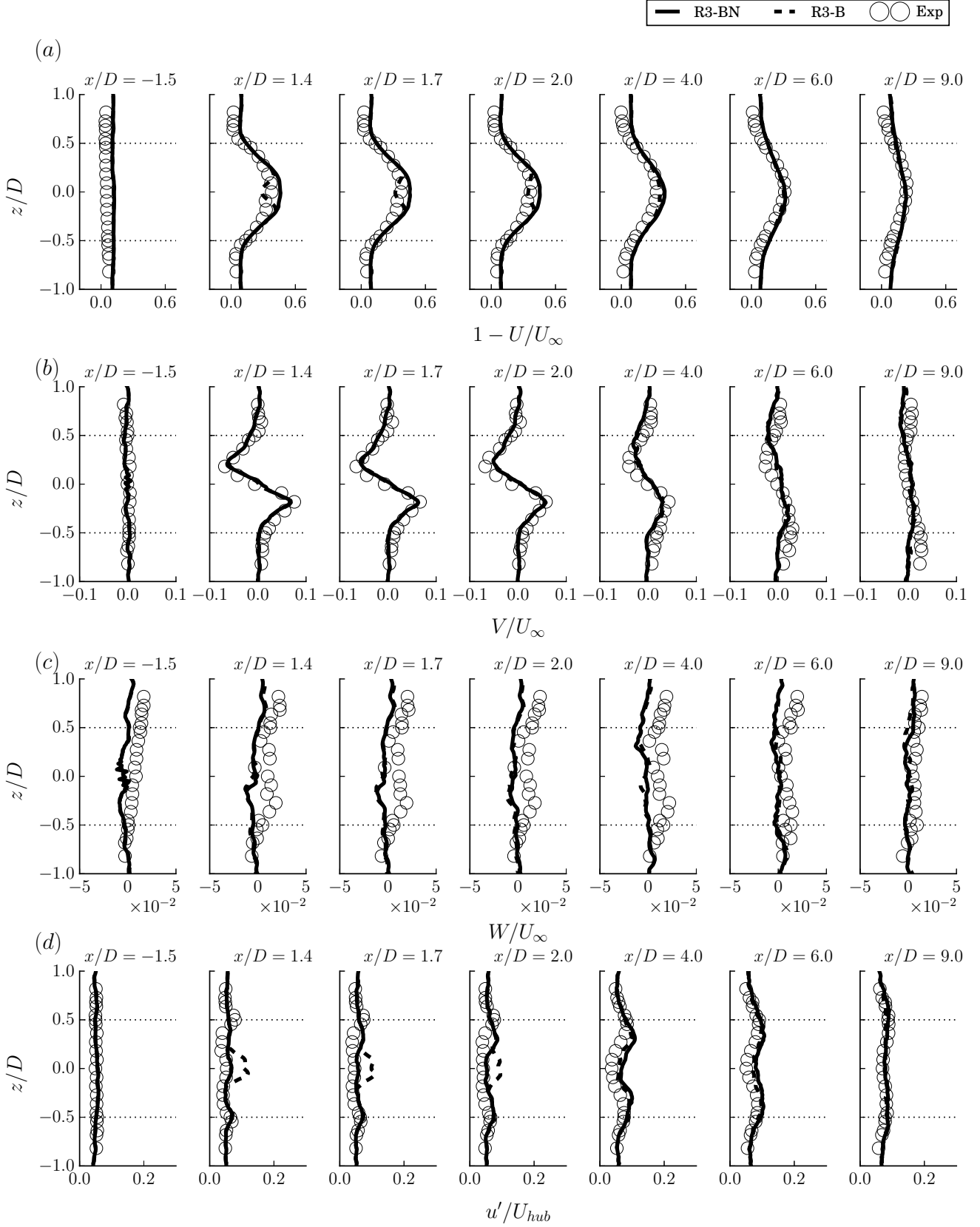


FIG. 7. Comparisons of the computed and measured spanwise profiles for the Region 3 case for (a) streamwise velocity deficit, (b) vertical velocity, (c) spanwise velocity, and (d) streamwise RMS velocity u' . The horizontal dotted lines at $z/D = \pm 0.5$ are the tip positions. The velocity is non-dimensionalized by U_∞ , the mean freestream velocity.

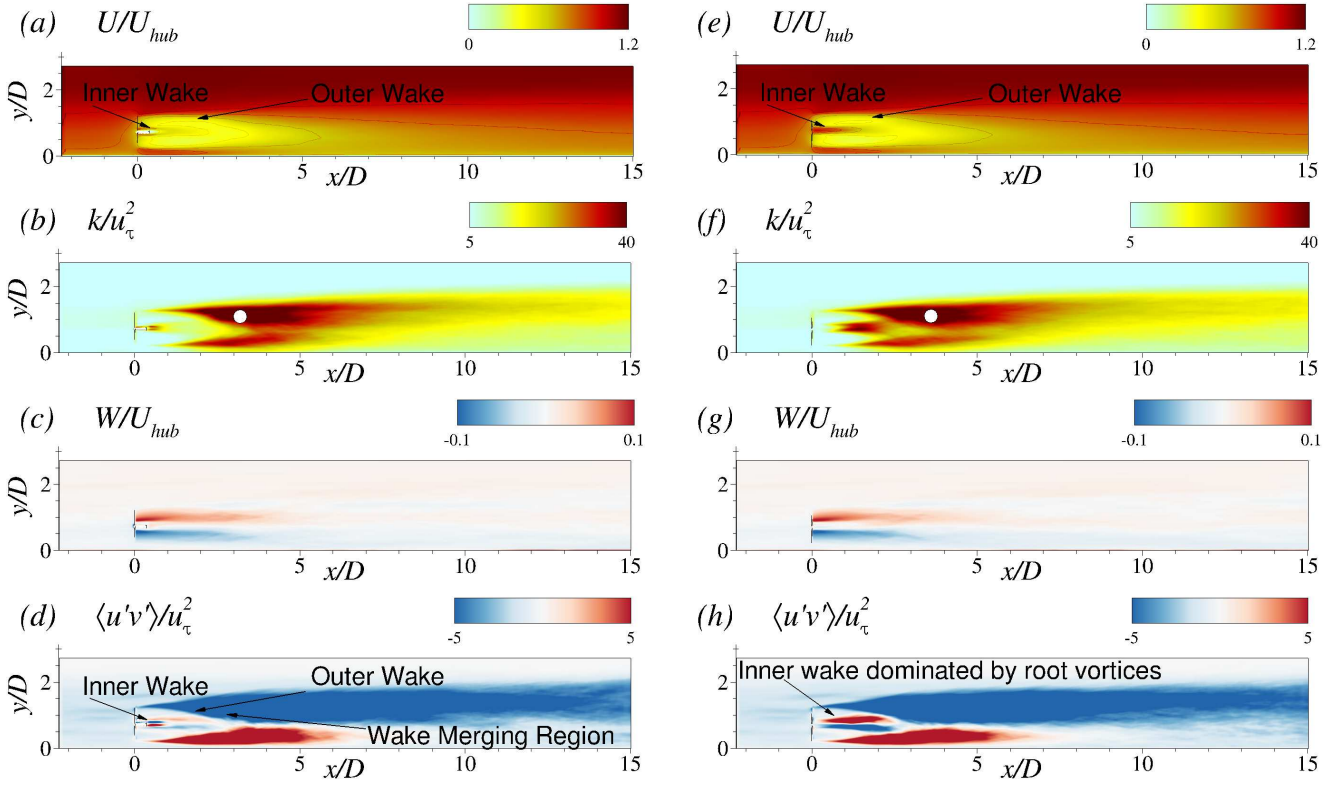


FIG. 8. Comparisons of vertical centerplane contours between simulations with (left images) and without (right images) a nacelle model for turbine operating in Region 2 for (a) and (e) time-averaged downwind velocity, (b) and (f) turbulence kinetic energy, (c) and (g) time-averaged spanwise (rotational) velocity, and (d) and (h) downwind-vertical Reynolds shear stress. Notations demarcating the inner wake (formed by the nacelle) and outer wake (created by rotor blades) are shown on Fig. (a), (d), and (h). Open circles in Figs. (b) and (f) indicate the location of maximum turbulence kinetic energy in the far wake.

iii.) Much like the TKE, there is a large region of high Reynolds shear stress that appears downstream along the tip positions and down towards the center of the wake. Here, in the wake merging region, the inner and outer wake merge together and intense mixing occurs. As the wake meandering region begins at approximately $x/D = 2$ downstream, the sign of the Reynolds stress indicates that slower moving fluid in the wake will mix and entrain fluid from the outer wake to initiate wake recovery. The streamwise-vertical Reynolds stress of the simulation without the nacelle model (Fig. 8(h)) provides more evidence of the strong columnar hub vortex which is dominated by strong Reynolds shear stress originating from the root of the turbine blades. While the Reynolds shear stress is relatively high in the inner wake, it is dominated by the root vortices which does not promote a similar laterally expanding inner wake from a nacelle as in the simulation with the nacelle model. The Reynolds shear stress from the root vortices indicates that mixing of the faster moving fluid from behind the turbine blades towards the centerline does not occur as effectively as in the simulation with a nacelle model. The centerline jet creates a non-physical acceleration of the streamwise flow promoting a stable columnar vortex. Further downstream, the increased Reynolds stress behaves similar to the nacelle model cases but with less turbulence mixing. Overall Reynolds shear stress comparisons of the simulations with and without nacelle suggest quantitative differences in the intensity of the far wake meandering region. This important issues will be discussed extensively in subsequent sections of this paper.

Figures 9(a)-(d) and Figs. 9(e)-(h) show contours of mean flow quantities for the turbine operating in Region 3 on the vertical-streamwise centerplane for simulations with and without a nacelle model, respectively. The mean streamwise velocity contours in Fig. 9(a) shows similar outer and inner wakes patterns as that in Fig. 8(a) for the turbine operating in Region 2. However, in comparison with that for the turbine operating in Region 2, the strength of the velocity deficit in the outer wake for the turbine operating in Region 3 is significantly less because of smaller power and thrust coefficients that resulted from the large pitch angle of the blade. The reduced velocity deficit enables faster recovery of the wake with less expansion in the radial direction for the Region 3 case. Similar to the Region 2 cases, lack of a nacelle model also results in an unphysical centerline jet which affects the wake development.

The TKE k/u_τ^2 contours are shown in Fig. 9(b) and Fig. 9(f), for simulations with and without a nacelle model,

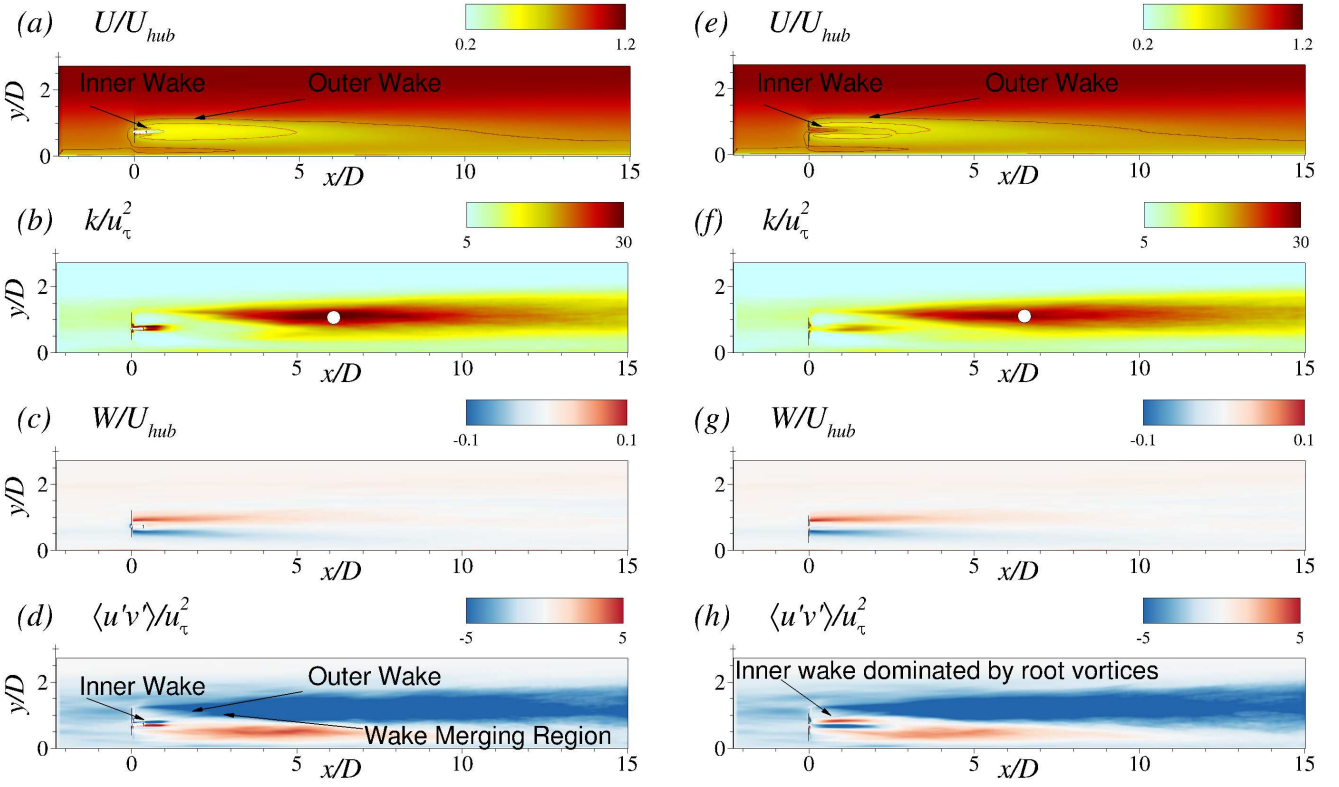


FIG. 9. Comparisons of vertical centerplane contours between simulations with (left images) and without (right images) a nacelle model for turbine operating in Region 3 for (a) and (e) time-averaged downwind velocity, (b) and (f) turbulence kinetic energy, (c) and (g) time-averaged spanwise (rotational) velocity, and (d) and (h) downwind-vertical Reynolds shear stress. Notations demarcating the inner (formed by the nacelle) and outer wake (created by rotor blades) are shown on Fig. (a). Open circles in Figs. (b) and (f) indicate the location of maximum turbulence kinetic energy in the far wake.

respectively. As seen, the maximum TKE in the top tip shear layer is higher and the region with high TKE is wider for the simulation with a nacelle model in comparison with that without a nacelle model. The location of maximum TKE occurs at $x/D = 6$ downstream for the simulation with a nacelle model, while the corresponding location for the simulation without a nacelle model occurs further downstream at $x/D = 6.5$. Comparing the TKE contours in Fig. 9(b) and Fig. 8(b) for the two operating conditions, we see differences in both the magnitude of the TKE and the downstream location where the highest TKE occurs. The region with high TKE for the turbine operating in Region 3 is longer and extends at further downstream locations but with significantly less maximum TKE in comparison with that in Region 2. The rotation of the wake for the turbine operating in Region 3, presented in Fig. 9(c) and Fig. 9(g), respectively, is more confined and with a comparably weaker maximum rotation. However, the mean rotation in the wake takes about the same distance or even somewhat longer distance from the rotor to dissipate. The streamwise-vertical Reynolds stress $\overline{u'v'}/u_\tau^2$ is consistent with the results from the turbine operating in Region 2, but with lower turbulence mixing levels due to less velocity deficit and weaker wake meandering as will be shown in section V.3.

Turbulence intensities at far wake locations can be considered as footprints of wake meandering. In order to further evaluate the operating regime and nacelle effects at far wake locations, we show in Fig. 10 different components of turbulence intensities at various downstream locations. For the Region 2 cases, the streamwise turbulence intensity computed from the case with a nacelle model is only slightly higher than that without a nacelle model at the $x/D = 3$ location. The differences are also minor for the other two components at $x/D = 3$ and 4 locations. At locations $x/D = 5$ and 8 the differences in the turbulence intensities of the cases with and without the nacelle model are negligible. For the Region 3 cases, the turbulence intensities computed from the simulation with a nacelle model is larger than that without a nacelle model especially near the hub height at the $x/D = 3$ location due to the formation of the unphysical hub vortex developed without a nacelle model. The differences at further downstream locations, on the other hand, are very minor. Comparing the turbulence intensities between the two different turbine operating conditions, we can see that at $x/D = 3$ and 4 locations, the turbulence intensities are larger for the Region 2 condition

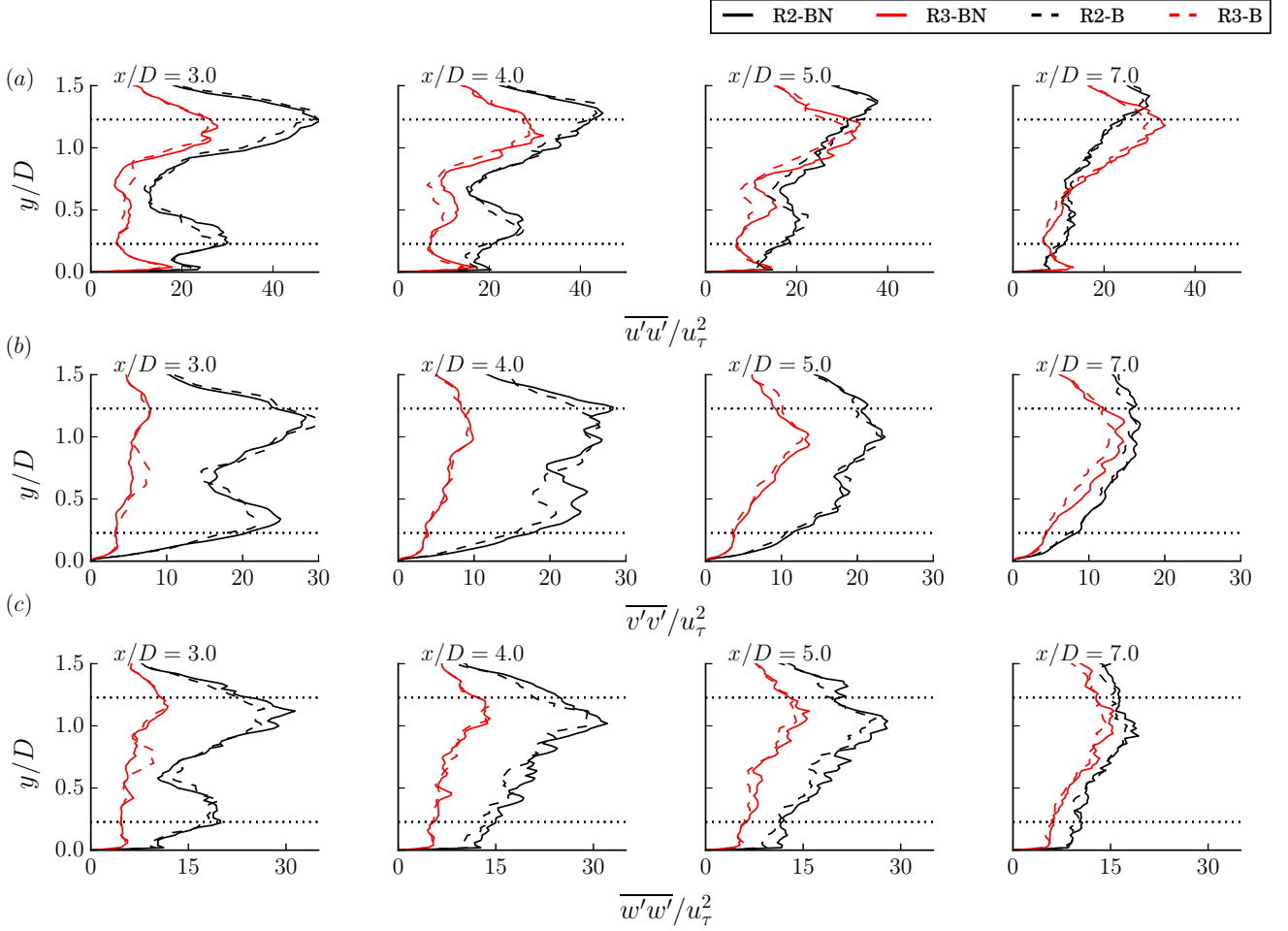


FIG. 10. Vertical profiles of the turbulence variances for (a) $\overline{u'u'}/u_\tau^2$, (b) $\overline{v'v'}/u_\tau^2$, and (c) $\overline{w'w'}/u_\tau^2$ non-dimensionalized u_τ^2 , where u_τ is the friction velocity of the incoming turbulent boundary layer flow. The horizontal dotted line show the bottom and top tip position at $y/D = 0.23$ and 1.23 , respectively.

for all the three components; at $x/D = 5$ and 7 locations; on the other hand, the streamwise turbulence intensity near the top tip location is larger for the Region 3 condition. Overall, Fig. 10 quantitatively indicates the significant effects of turbine operating condition on turbulence intensity at far wake locations for this model wind turbine.

V.2. Instantaneous flow fields and spectral analysis

In this section, we focus on the instantaneous flow fields to get an intuitive cognition on the different wake meandering patterns for different operating conditions and simulations with and without a nacelle model. The analysis of the mean flow field demonstrated that both the inner wake and outer wake form behind the turbine. In the mean sense, the inner wake expands into the outer wake and the turbulence kinetic energy increases substantially downstream. To further investigate the instantaneous evolution of the wake and substantiate the narrative presented above, several time instances of both operating conditions from the simulations with a nacelle are shown in Fig. 11. Each successive instance is separated by one rotor rotation period $T = 0.07$ s. The instantaneous flow field from the Region 2 case, in Fig. 11(a), contains an inner wake with flow reversal directly behind the nacelle and a large outer wake extending from the extent of the rotor blades. Over the successive figures the slow precession of the hub vortex and the expansion of the inner wake becomes evident. Around $x/D = 2$, the inner wake begins to interact with the outer wake, and large lateral excursions of the outer wake mark the onset of the meandering. By $x/D = 4$ the full extent of the wake

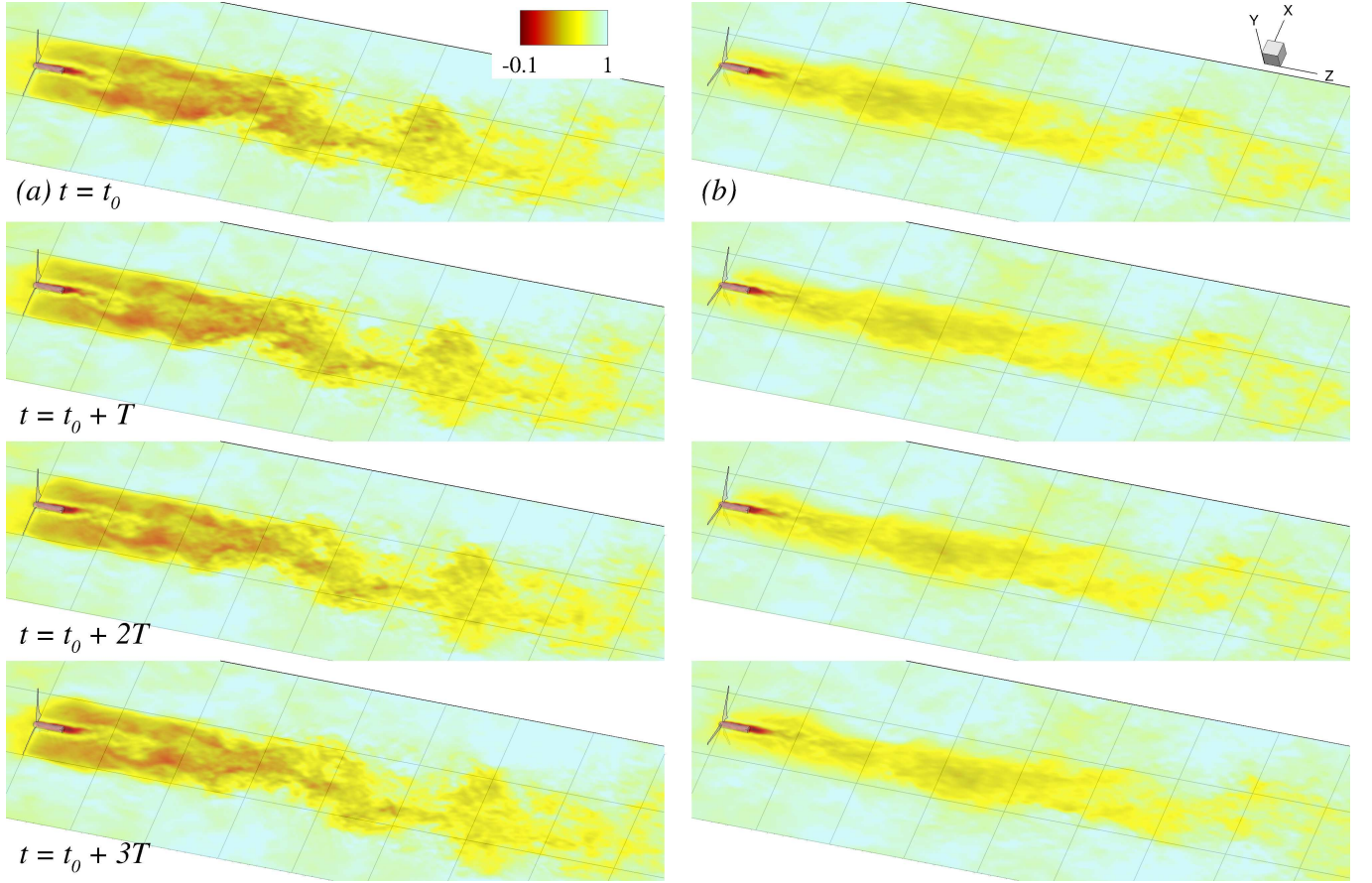


FIG. 11. Contours of the instantaneous streamwise velocity normalized by U_{hub} at four successive time instances for (a) turbine operating in Region 2 (R2-BN) and (b) turbine operating in Region 3 (R3-BN).

meandering has commenced. After the emergence of the meandering, progressively larger spanwise displacements of the wake around the streamwise velocity minimum locations occurs. The locus of the velocity minima along the streamwise direction define a helical centerline of the meandering wake. Over a period of 4 rotor rotations, the wake meandering convects downstream, and the amplitude grows. A slightly different wake evolution is seen in Fig. 11(b) for the Region 3 case. Both the inner wake hub vortex core with helical precession and outer wake form but remain more columnar. As discussed before, due to the blade pitch the outer wake is weaker compared to Region 2. The outer wake remains columnar with slight distortions from interactions outside the wake while the inner wake slowly expands. The onset of wake meandering does not occur until after $x/D = 5$.

Similar instantaneous snapshots of the streamwise velocity for the simulations for both turbine operating conditions without a nacelle are shown in Fig. 12. Close to the turbine, a jet along the centerline is clearly evident in both simulations. Instantaneously, the near wake region transitions into wake meandering near the same distance from the turbine.

Figure 13 shows comparisons of the measured and simulated Fourier power spectral density of the streamwise component of the velocity fluctuations at the top tip position at several locations in the wake for both operating conditions. The non-dimensional frequency Strouhal number $St = fD/U_{hub}$ is defined by the turbine diameter D and hub height velocity U_{hub} . The experimental data collected used to create the power density spectra are captured over a runtime of 850 rotor revolutions with time step $dt = T/70$, where T is the turbine period, while the simulation data are captured over a 275 rotor revolution runtime with a time step $dt = T/360$. With the duration of the data collection and the time step, the power density spectra are observed to be converged within the frequency range $0.1 < St < 3.0$ for both the experimental and simulation data. At $x/D = 2$, the measured spectra shows that there are peaks at $St = 2.3$ and $St = 0.8$ and a longer flat region in low frequency space. The former peak is the rotor frequency and is also present in the simulation results. Both signatures are muted in the Region 3 cases. A lower frequency around $St \sim 0.2 - 0.3$ is present Fig. 13(b), Fig. 13(c), and Fig. 13(d). The low frequencies are found in both measurements and simulations and are stronger in the simulations that include a nacelle model. Farther

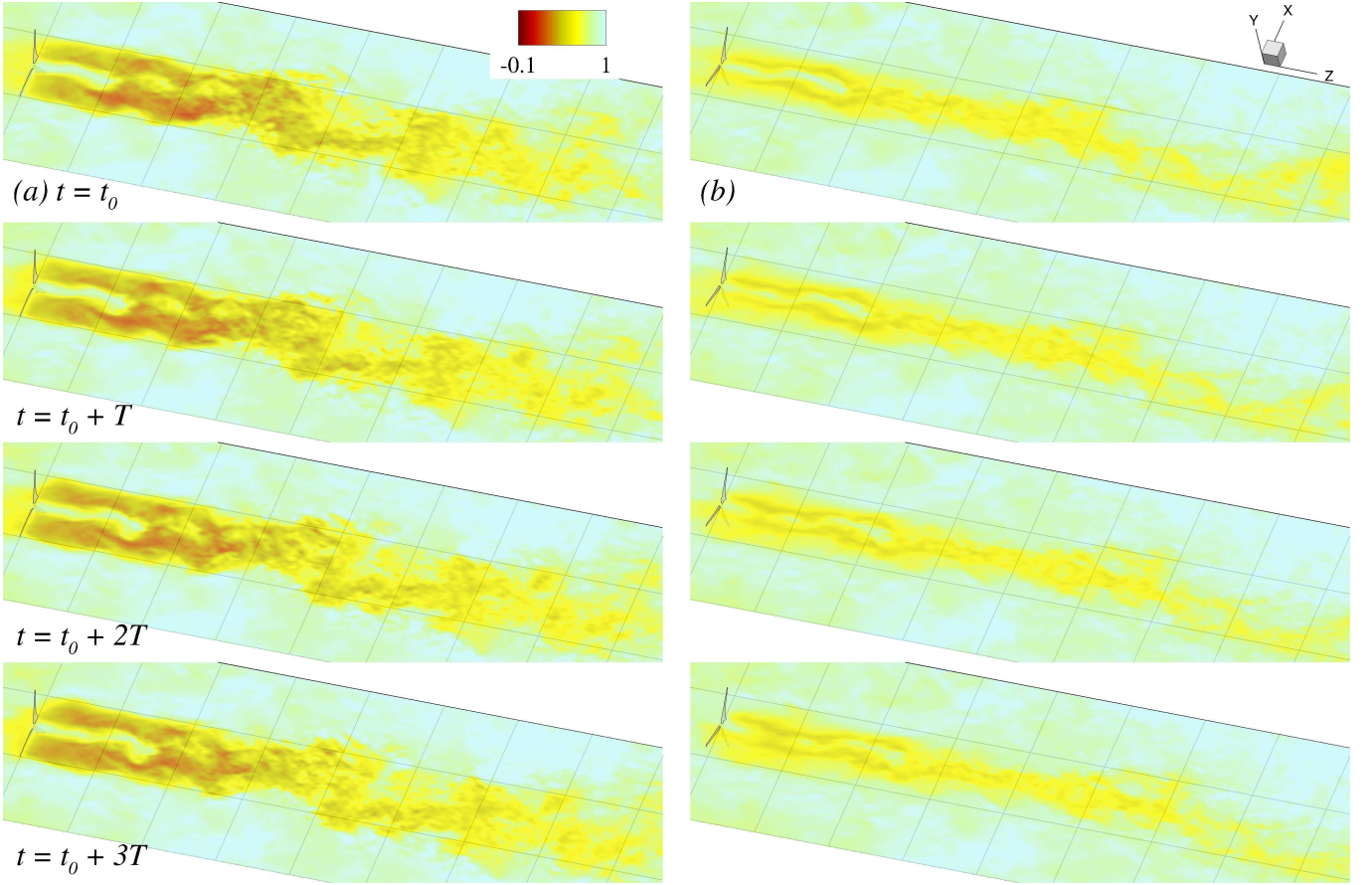


FIG. 12. Contours of the instantaneous streamwise velocity normalized by U_{hub} without a nacelle model at four instantaneous time instances for (a) turbine operating in Region 2 (R2-B) and (b) turbine operating in Region 3 (R3-B).

downstream the high frequencies in computed spectrum have slightly more energy possibly due to the LES not having sufficient grid resolution to adequately capture the high frequency modes. However, the processes we are concerned about are the low frequency modes, which will be discussed below. The energy in these frequencies is similar to the measured data.

Figure 13(b) at $x/D = 4$ shows the simulation with a nacelle model turbine operating Region 2 has more energy in the low frequency energy modes than the simulation without a nacelle. At $x/D = 6$ and 9 locations in Fig. 13 the low frequency modes have similar energy consistent with the streamwise turbulence intensities in Fig. 10 at $x/D = 5$ and 7 locations. In the turbine operating Region 3, the energy for simulations with a nacelle model in the low frequency modes at locations $x/D = 4, 6$ and 9 is higher than simulations without a nacelle. The energy differences are another indication that without a nacelle the turbulent energy at low frequencies is reduced. This further shows that the nacelle model is necessary for accurate simulations of a wind turbine. Without it, the high energy, low frequency contributions cannot be fully taken into account.

The contours on the $St-x$ plane of Fourier power spectral density of the streamwise component of the velocity fluctuations pre-multiplied by frequency $f\Phi_{11}$ for the simulations with the nacelle model are shown in Fig. 14 for three different radial locations. This allows us to visualize the evolution of the frequency modes in the wake of the turbine. Starting at the centerline $y_h = y - H = 0$, there are several frequency regions of high energy. Nearest to the turbines, $x/D = 0.5$, a high energy mode is centered around $St = 0.7$. Given the proximity to the turbine along the centerline, this is immediately recognized as the hub vortex. The Strouhal number is similar to the measured hub vortex frequencies of other turbines [20–22, 26]. In the Region 2 case, the peak hub vortex energy occurs directly downstream of the turbine and quickly dissipates. By $x/D = 2$, the energy level has dropped significantly, but, relatively, it is the strongest energy mode in the flow at that axial location. This indicates that the hub vortex contains most of the energy along the centerline. However, after $x/D = 2$ another, lower, frequency mode becomes present, the wake meandering frequency, most prevalent at $St = 0.3$, which has been observed in numerous studies: $St = 0.23$ [19], $St = 0.28$ [25], $St = 0.15$ [22] and $St = 0.15 - 0.25$ [24]. Both the wake meandering frequency and the hub vortex

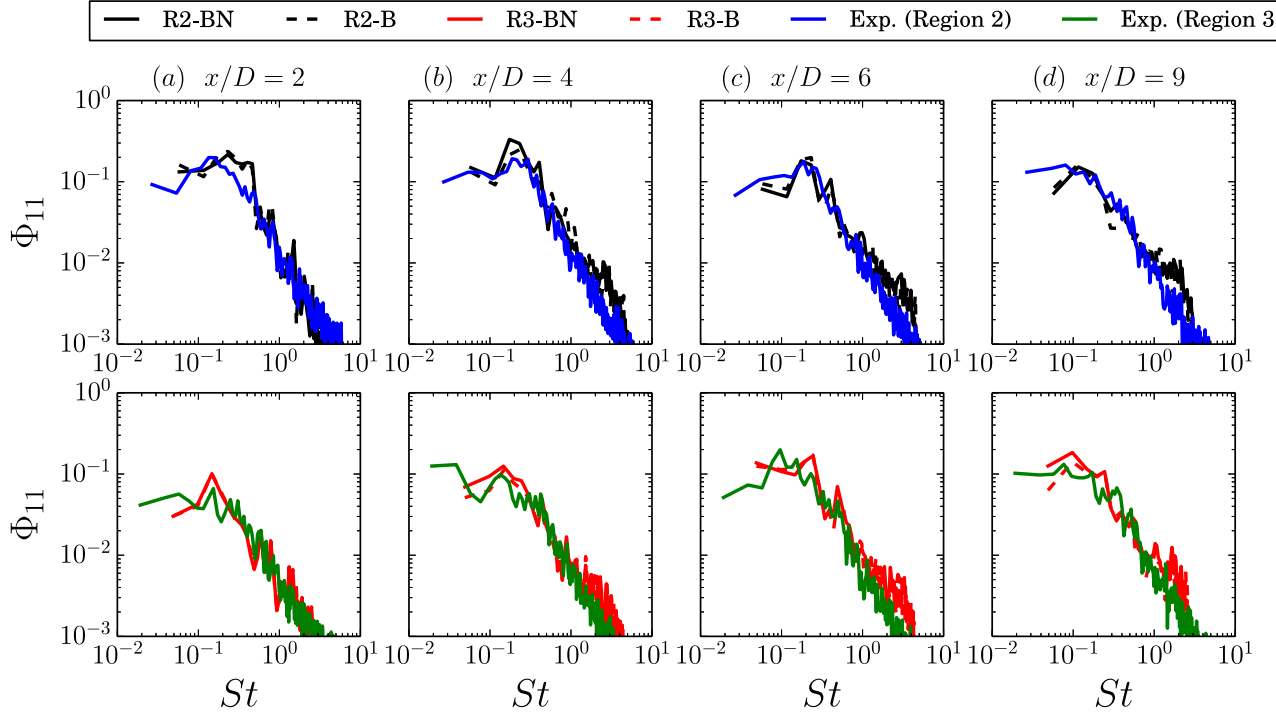


FIG. 13. Comparisons of the Fourier power spectral density of the streamwise component of the velocity fluctuations Φ_{11} with that from measurements, with the top images and bottom images in Region 2 and Region 3, respectively, along the tip position $y/D = 0.72$, and $z/D = 1$ for (a) at $x/D = 2$, (b) at $x/D = 4$, (c) at $x/D = 6$, and (d) at $x/D = 9$.

frequency remain the dominant frequencies throughout the rest of the domain along the centerline, a clear indication that while the hub vortex breaks down, its remnants continue to affect the flow far downstream. The centerline frequency contours of Region 3 have some drastic distinctions from the former case. Here, the hub vortex energy peaks further from the rotor. Between $2 < x/D < 4$, little low turbulent energy is present indicating the hub vortex has not broken down and no interaction with the outer wake has occurred. By $x/D > 6$, further downstream than that of Region 2 and consistent with mean turbulent statistics, the wake meandering mode is activated. Moreover, the interaction between the inner and outer wake not only affects the wake meandering but also strengthens the hub vortex frequency mode along the centerline very close to the turbine.

In both cases near the mid-blade location, $y_h/D = 0.2$, the hub vortex frequency is not distinguishable from other frequency modes close to the turbine. Further downstream, the wake meandering frequency appears, first in Region 2 at $x/D = 2.5$, consistent with the turbulence kinetic energy shown above. The peak wake meandering energy occurs around $x/D = 4$, and high energy is observed far downstream as the wake meanders throughout the far wake. For Region 3 case, the wake meandering is observed to peak much further downstream, around $x/D = 5$ and is also present far downstream. The energy present in the wake meandering mode at this radial position is higher compared to the centerline. Here, there is more turbulence energy in the wake meandering mode in the wake because of the proximity to the location of the interaction of the expanding inner wake and outer wake. Near the peak wake meandering location, higher frequency modes are also present and can be attributed to the complex interaction of the inner wake including the hub vortex with the outer wake.

Closer to the blade tips at $y_h/D = 0.44$, similar to the mid-blade location, the hub vortex frequency is not present near the turbine. Higher frequencies associated with the rotor frequency and the tip vortices are present but quickly dissipate and become indistinguishable compared to wake meandering. Consistent with the findings of the turbulence kinetic energy and the mid-blade power density spectrum, wake meandering in Region 2 begins earlier than in Region 3. The peak energy levels are slightly upstream compared with the mid-blade and centerline. Turbulence energy in the outer wake is highest due to the strength of the tip shear layer and interaction with the hub vortex core formed behind the rotor. From these contours, we conclude that wake meandering begins at the outer wake, and the interaction of the inner wake with the outer wake introduces more turbulence. Evidence from streamwise power spectra in Fig. 13 shows that without the expanding inner wake the energy of the wake meandering is diminished. From

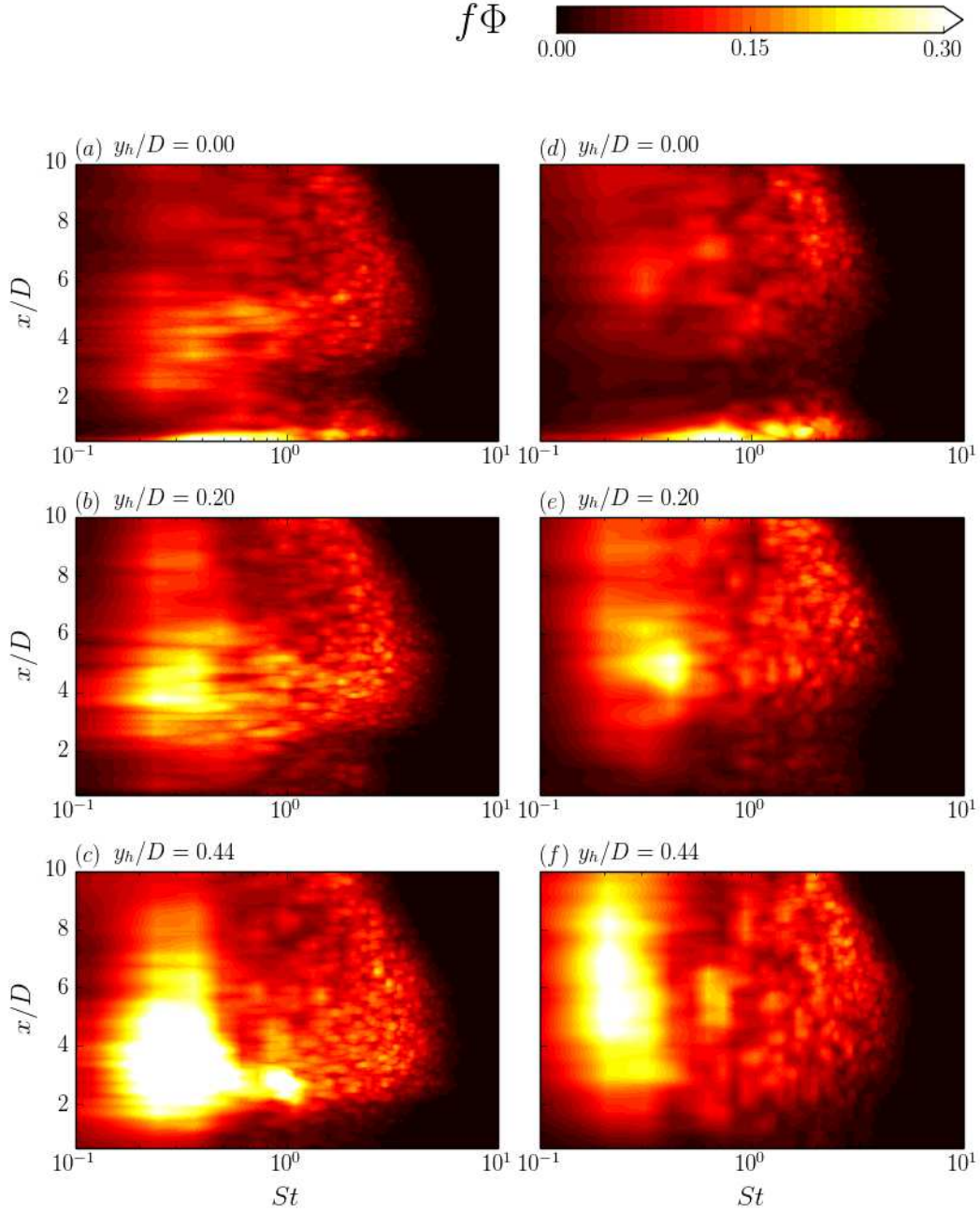


FIG. 14. Contours of the Fourier power spectral density of the streamwise component of the velocity fluctuations pre-multiplied by frequency $f\Phi$ as a function of the axial direction, x/D at several radial positions (a),(d) $y_h/D = 0$, (b),(e) $y_h/D = 0.2$ (c),(f) $y_h/D = 0.44$. Left column (a)-(c): R2-BN and right column (d)-(f): R3-BN.

onset of the wake meandering in the outer wake shear layer, the meandering modes begins to propagate downstream and towards the centerline explaining why the centerline energy peak of wake meandering occurs slightly further downstream compared to the top tip location.

V.3. Meander Profiles

In this section, analysis is performed by reconstructing instantaneous wake meandering into meander profiles that track the streamwise velocity minimum locations to further understand the dynamics of the wake of the turbine. Previous studies have attempted to track the mean and instantaneous wake of wind turbines by tracking the mid-point of the wake [70], center of mass [71] and Gaussian modelling [72, 73]. In this study we strive to reconstruct the instantaneous path of the wake meandering through a spatio-temporal filtering technique. In the instantaneous contours, Fig. 11, we observe that in general lower streamwise velocity is located near to center of the meandering wake. By tracking the minimum streamwise velocity positions with a three-dimensional profile, we investigate the dynamics in terms of amplitude and wavelength of meanders and obtain statistics of the dynamical wake. The reconstruction technique was first described in Howard *et al.* [26] and developed for temporal and spatial resolved three-dimensional LES flow field in Foti *et al.* [22]. A three step procedure is utilized for the three-dimensional helical meandering profile reconstruction: i) use finite temporal average scheme proposed by Chrisohoides and Sotiropoulos [74] to find the coherent time scale τ_c of the wake, ii) locate the streamwise velocity minima along the axial direction, iii) spatially filter the velocity minimum locations to create a continuous profile.

The proposed method for reconstruction of the wake meandering is based on tracking wake meandering as a large-scale coherent structure in the wake of the turbine. The flow field is temporally filtered to eliminate the high frequency fluctuations which are not associated with the low frequency wake meandering. The temporal filtering process uses finite averaging over a coherent time scale τ_c to decompose the flow field into the usual triple decomposition of a turbulent flow as described by Hussain [75]. A temporally and spatially evolving flow field $\mathbf{u}(\mathbf{x}, t)$ (bold indicates a vector quantity) can be rewritten as follows:

$$\mathbf{u}(\mathbf{x}, t) = \mathbf{U}(\mathbf{x}) + \tilde{\mathbf{u}}(\mathbf{x}, t) + \mathbf{u}_i(\mathbf{x}, t), \quad (10)$$

where $\mathbf{U}(\mathbf{x})$ is the mean, strictly spatial term, $\tilde{\mathbf{u}}(\mathbf{x}, t)$ is the coherent term and $\mathbf{u}_i(\mathbf{x}, t)$ is the incoherent term. Based on the work of Chrisohoides and Sotiropoulos [74], the optimal size of an interval averaging window is equivalent to the coherent time scale and can be determined by starting with a finite averaging over a time window of τ as follows:

$$u_\tau(x, t) = \frac{1}{\tau} \int_{t-\tau/2}^{t+\tau/2} u(x, t') dt'. \quad (11)$$

The proper coherence time scale can be found by employing fluctuation analysis and the central limit theorem. Using a τ too small the large-scale motions will be dominated by incoherence, while averaging over too long will smear out the coherent structures. Fluctuation analysis shows that the coherent time scale τ_c is the time window where the standard deviation over the temporal window begins to scale as $\tau^{-1/2}$. With this temporal window, the finite averaged velocity $u_\tau(x, t) = U(x) + \tilde{u}(x, t)$. For more background, see Chrisohoides and Sotiropoulos [74] and Foti *et al.* [22]. The optimal coherent time scale for all cases is found to be about $\tau_c = 0.6T$. This value is close to the optimal time scale of a model turbine discussed in Foti *et al.* [22].

The present analysis will only be considered on the instantaneous LES flows which have adequate spatial and temporal resolution over 200 rotor revolutions. Similar data is not available for the present experiments where data is only known at the discrete measurement points shown in Figs. 6 and 7.

With the coherent time scale determined and the flow decomposed into its three parts, the minimum streamwise velocity, $U(x) + \tilde{u}(x, t)$, locations along the axial direction are tracked at the coherent time scale resolution. Physically, the velocity minima track near the center of the hub vortex near the turbine and meandering in the far wake. A low-pass spatial filter using a length scale $l_c = D/2$ is used to obtain a three-dimensional continuous profile out from the velocity minima, as shown in Howard *et al.* [26].

Figures 15(a)-(d) show examples of a three-dimensional meander profile projected on the hub height plane for both turbine operating conditions and simulations with and without the nacelle model. In each figure, the solid line represents the meandering profile, and the circle markers are the velocity minimum locations in the wake. The meander profile is superimposed on the instantaneous vorticity magnitude, $|\omega|D/U_{hub}$. The trends addressed previously in the instantaneous streamwise snapshots in Fig. 11 about the dynamics of the wake for each case are observed in the meander profiles. In Fig. 15(a), the snapshot of the meander profile of the simulation with a nacelle model for the turbine operating in Region 2 shows an energetic wake and the meander profile that starts behind the nacelle and quickly expands tracking the hub vortex toward the outer wake. Accompanying the expansion of the hub vortex and increasing amplitude of the meander profile is an increased vorticity magnitude near the peaks of the meander profile at the tip shear layer (shown by dashed lines on the Figures 15(a)-(d)). This is further evidence that the expansion of the hub vortex towards the tip shear layer occurs with increases in turbulence intensity as the tip shear layer and hub vortex interact as the meandering of the wake commences. Figure 15(b) shows the snapshot of the simulation without a nacelle model in Region 2. The meander profile cannot start immediately downstream of the rotor because

the centerline jet affects the location of the velocity minima near the turbine. The meander profile starts at $x/D = 3$ where the centerline jet dissipates. A meander profile of the Region 3 simulation with a nacelle is observed in Fig. 15(c). Unlike Region 2 simulations, the inner wake is less energetic, and the meander profile is a tight spiral for 5 diameters behind the turbine. After $x/D = 5$ the meander profile has large amplitudes towards the tip shear layer. Similar to Region 2, instantaneous high vorticity regions are near the peaks of the meander profile. The simulation without the nacelle model operating in Region 3 is shown in Fig. 15(d), with similar trends as the simulation with the nacelle model. Further analysis of many meanders is necessary to understand the trends in the wake.

The statistics of the meander profiles are useful in determining the dynamics of the hub vortex and wake meandering. It is useful to investigate the wave-like characteristics, amplitude and wavelength, of the meander profiles as a function of axial distance from the turbine. The behavior of amplitude and wavelength can be interpreted in both the near wake and far wake separately. In order to obtain the wave features, the three-dimensional helical profile is projected onto the two-dimensional hub height plane where amplitudes A and wavelengths λ are readily calculated from the extrema of the profile. In Fig. 15(e), the average amplitude \bar{A}/D as a function of the downstream distance for each test case is shown. In the simulation with a nacelle model in Region 2, the amplitude quickly increases behind the turbine with the expanding hub vortex. By $x/D = 2$ the amplitude increases to a peak in the near wake followed by a plateau as hub vortex interacts with the outer wake. The amplitude increases further as the wake begins to meander. On the other hand, in Region 3, the amplitude is much lower in the near wake, consistent with the tight spiraling hub vortex. The amplitude increases linearly until $x/D = 5$ where the wake meandering commences. The average amplitude in Region 3 remains lower than the amplitude in Region 2 throughout the wake. This is consistent with linear stability analysis performed by Ashton *et al.* [42] which indicated that both increasing the tip-speed ratio and decreasing the wind turbine loading reduce the growth rate of the hub vortex instability. Simulations without the nacelle yield meander profiles with lower amplitudes regardless of turbine operating condition. In Region 2, the average amplitude between the simulations with and without the nacelle model remains similar until $x/D = 4.5$ where the differences becomes more pronounced. The amplitude is more attenuated for the simulation without a nacelle in Region 3 starting from $x/D = 5$ where wake meandering is witnessed to commence. We can relate the amplitude A to the energy E of the meander profile, $A^2 \sim E$. Consistent with the power spectrum in Fig. 13, the energy in the wake meandering is reduced by up to 40% without a nacelle model far from the turbine, $x/D > 5$ regardless of the operating regime. Figure 15(e) provides quantitative evidence that a nacelle model is needed to adequately simulate the dynamics of the wake.

The average wavelength $\bar{\lambda}/D$ of the meander profiles is shown in Fig. 15(f). Unlike the amplitudes for each case, the average wavelength is approximately the same regardless of the nacelle model. The similarity of the profiles is indicative that the wavelength is a large-scale feature of the flow not pertaining to the dynamics. For all cases in the far wake, the mean recovery of the wake is generally the same. The evidence shows that the mean elongation of the meandering profile is caused by the wake of the turbine. As the wake recovers, the meander is stretched in the streamwise direction.

The statistics of the meander profiles are further investigated in Fig. 16 with the probability density function (PDF) of the amplitude and the wavelength shown at different locations downstream. The amplitude PDF for the simulation with a nacelle model in Region 2 flattens as the location from the turbine increases. At $x/D = 2$ the highest amplitudes extends only $A/D = 0.15$. The maximum amplitudes eventually extend beyond $A/D = 0.25$, indicating that the centerline of the wake is being displaced out to the tip shear layer by wake meandering. Conversely, the amplitude PDF of the simulation with a nacelle model in Region 3 has both a lower median and standard deviation than in Region 2. The standard deviation of the amplitude normalized by the average amplitude σ_A/\bar{A} , an indication of the uncertainty in the amplitude, is nearly constant throughout the domain and in all simulations around 0.7. At $x/D = 2$ location, the PDF is narrow, consistent with the tightly spirally hub vortex. At locations further downstream, the amplitudes increase but the maximum in Region 3 is always less than in Region 2. With regards to the simulations without a nacelle mode, they are not shown at $x/D = 2$ due to the manifestation of the unphysical centerline jet which affects the location of the velocity minima in the inner wake. At locations further downstream, the simulations without the nacelle have slightly lower amplitude medians than the corresponding simulation with nacelle model. The maximum amplitudes achieved are also lower.

The PDFs of the wavelength show a gradual growth of the median and variance as the locations from the turbine get further downstream. At $x/D = 4$, most wavelengths for all cases are near $\lambda/D = 1$. By $x/D = 8$, the wavelengths increase significantly and the PDFs all have a flattened peaks from $1 < \lambda/D < 3$. Although the wavelength PDFs of simulations with a nacelle model far from the turbine have a slight shift towards higher wavelengths, the wavelength for both operating conditions and nacelle model are not substantially different.

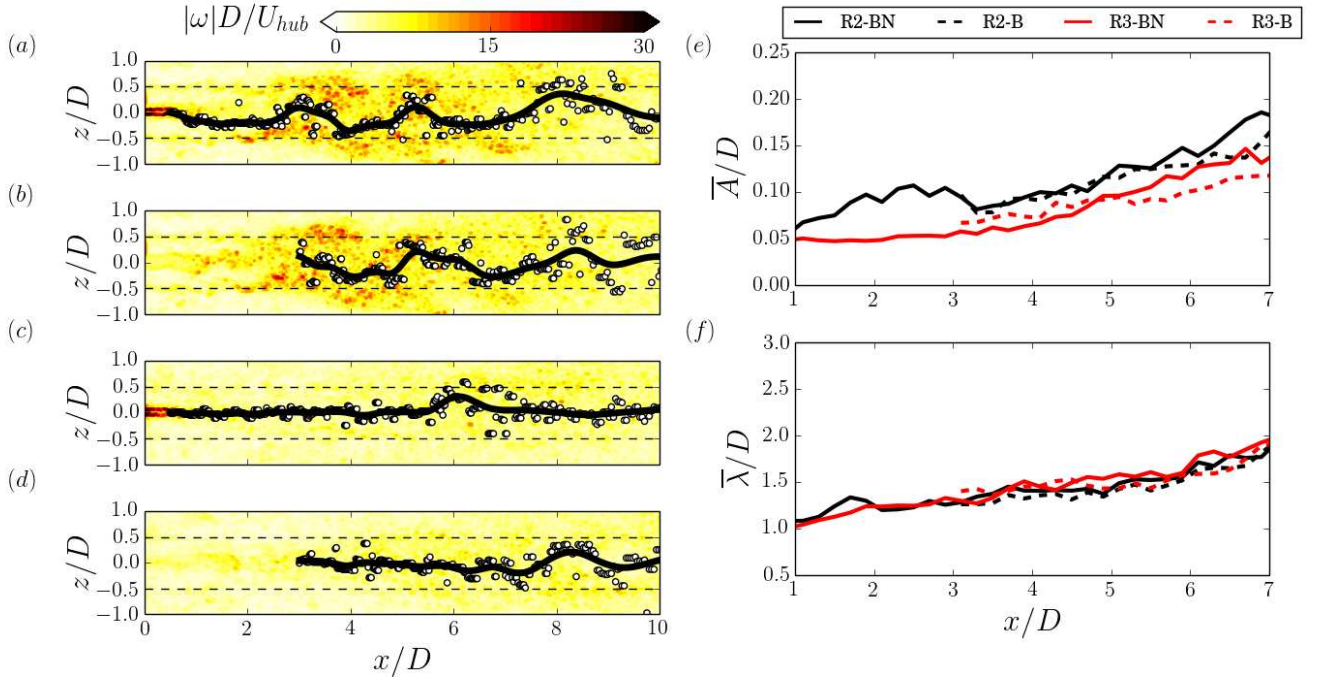


FIG. 15. Instantaneous vorticity magnitude, $|\omega|D/U_{hub}$ with velocity minima (dot) and meander profile (line) for (a) R2-BN, (b) R2-B, (c) R3-BN, (d) R3-B. Average meander profile (e) amplitude, \bar{A} , and (f) wavelength $\bar{\lambda}$ with respect to distance from rotor plane, x/D , non-dimensionalized by the diameter D .

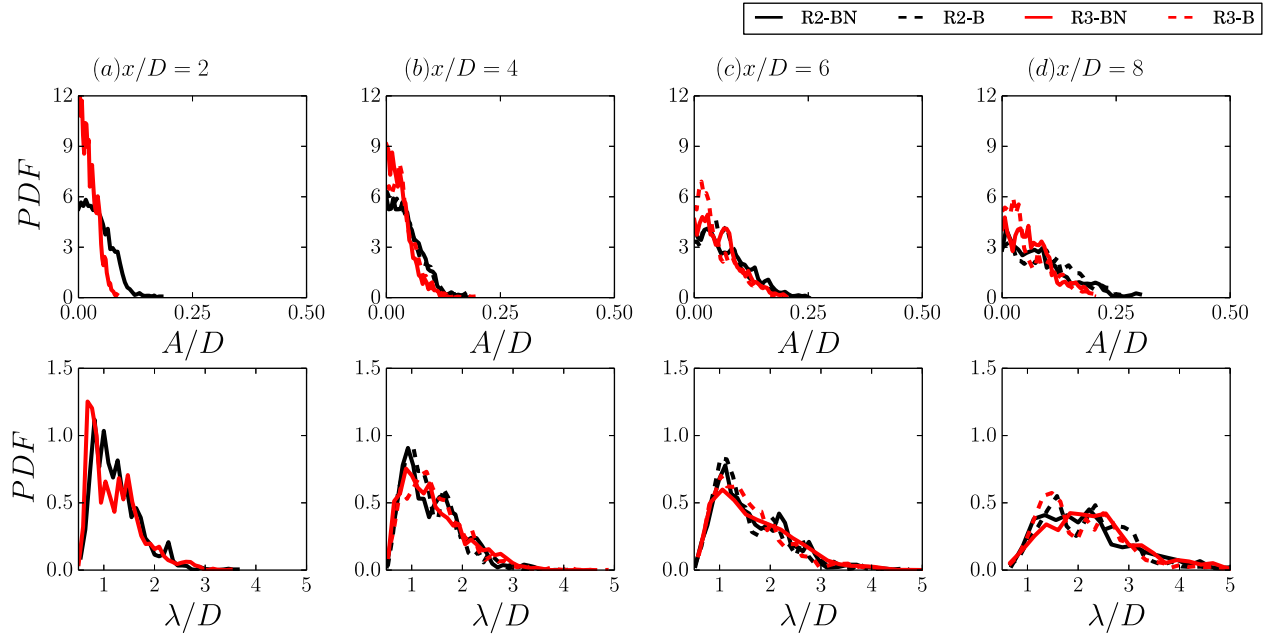


FIG. 16. Probability density function of the amplitude, A/D (first row) and wavelength, λ/D (second row) of the meander profiles at (a) $x/D = 2$, (b) $x/D = 4$, (c) $x/D = 6$, and (d) $x/D = 8$.

V.4. Dynamic Mode Decomposition and Meander Profile

Up to this point, we have concentrated the development of two large coherent structures in the wake: the hub vortex and wake meandering. Each structure is associated with a dominant frequency, and the dynamics is interpreted through the meander profiles reconstruction. To further elucidate these coherent structures and their effect on the wake of the turbine, we decompose the wake using dynamic mode decomposition (DMD). DMD was first theoretically introduced by Rowley *et al.* [76] as a technique to decompose the flow by spectral analysis of the Koopman operator, a linear operator associated with the full non-linear system. The Arnoldi-like method was improved by Schmid [48] and is able to compute the modes of a finite sequence of snapshots of the flow field. Sarmast *et al.* [17] used DMD to separate wind turbine tip vortex modes for analysis. The modal decomposition is able to extract spatial structures and their corresponding frequencies and growth rates without having the explicit dynamic operator. Because DMD can separate specific spatial modes by their individual frequencies, we can explicitly extract the modes related to the hub vortex and wake meandering. With the spectral analysis performed above, the specific frequencies of the hub vortex and meandering wake are readily known from Fig. 14.

First, we will give a brief overview of the algorithm. For more information, please see Schmid [48] and Sarmast *et al.* [17]. For our simulations, a sequence of three-dimensional instantaneous flow fields $\mathbf{u}_i(\mathbf{x}_j, t_i)$, $t_i = i\Delta t$, $i = 0, 1, N - 1$ are assembled into a matrix

$$U_n = [\mathbf{u}_0, \mathbf{u}_1, \dots, \mathbf{u}_{N-1}], \quad (12)$$

where N is the number of snapshots, and Δt is the time between each snapshot. In DMD, a linear mapping A or \tilde{A} is assumed to relate a flow field \mathbf{u}_j to the succeeding flow field \mathbf{u}_{j+1} such that

$$\mathbf{u}_{j+1} = A\mathbf{u}_j + \epsilon e^T = e^{\tilde{A}\Delta t}\mathbf{u}_j + \epsilon e^T, \quad (13)$$

where ϵ is the residuals and $e = [0, \dots, 0, 1]^T$ and decomposing the flow field into spatial eigenmodes $\phi_k(\mathbf{x}_j)$ and temporal coefficients $a_k(t_i)$

$$\mathbf{u}_{j+1} = \sum_{k=0}^{N-1} \phi_k a_k = \sum_{k=0}^{N-1} \phi_k e^{i\omega_k \Delta t} = \sum_{k=0}^{N-1} \phi_k \lambda_k^j, \quad (14)$$

where the $i\omega_k$ is the corresponding eigenvalues of \tilde{A} , and λ_k^j is the corresponding eigenvalues of A . The amplitude d_k and energy d_k^2 of spatial dynamic mode ϕ_k are related such that $\phi_k = d_k \mathbf{v}_k$ where $\mathbf{v}_k^T \mathbf{v}_k = 1$. The eigenvalues λ_k , also referred to as the Ritz values, are complex conjugates which all lie on the complex unit circle, $|\lambda_k| = 1$. To obtain the more familiar complex frequency $i\omega_k = \log(\lambda_k)/\Delta t$. The real part is the temporal frequency, and the imaginary part is an exponential growth rate of the dynamic mode.

A substantial number of three-dimensional instantaneous snapshots are saved for each simulation in order to cover the amount of time needed to resolve the low frequencies of the hub vortex and wake meandering. Each snapshot contains the computational cells that are within a diameter wide and high box centered on the turbine and entire length of the computational domain. The mean flow is subtracted from each snapshot to obtain the fluctuating part of the flow field. The minimum time between the snapshots $\Delta t = T/12$, where T is the rotor period, a time difference low enough to ensure that not only the low frequency modes but the blade rotation frequency are captured as well. To ensure convergence of mode decomposition, the number of snapshots used are increased until the norm of the residuals, ϵ , of the mapping operator becomes sufficiently small. Figure 17(a) shows the residuals decrease by several orders of magnitude as the number of snapshots is increased to $N = 512$. Based on the residuals, the number of snapshots used for subsequent analysis will be $N = 512$. Moreover, several series of snapshots are used and averaged so the modes and frequencies are averaged over a time spanning $100T$. With a $\Delta t = T/12$ and $N = 512$, the low frequency precession of wake meandering occurs as many as five times which provides adequate temporal resolution for our proposes.

The energy d_k^2 and its frequency $St = \Re(2\pi i\omega_k)D/U_{hub}$ of k th mode for simulations with the nacelle model in Region 2 and Region 3 is shown in Fig. 17(b) and Fig. 17(c), respectively. The energy of each mode is normalized by the maximum energy. The maximum energy is associated with the wake meandering frequency $St = 0.3$. Also included in each figure are two normalized energy spectra: one located in the near wake at $x/D = 2$ and one located the far wake at $x/D = 5$. Both energy spectra have a maximum energy at $St = 0.3$ (Note both the extrema of energy of dynamic modes and the energy spectra occur at the same frequency). A few energy peaks are present in the DMD. In the low frequency region, $St < 1$, the dynamic mode energy peaks at the aforementioned $St = 0.3$ and $St = 0.74$, similar frequencies to what was determined to be the wake meandering frequency and hub vortex frequency, respectively. The energy spectra confirm that DMD decomposes the flow field into modes corresponding to modes

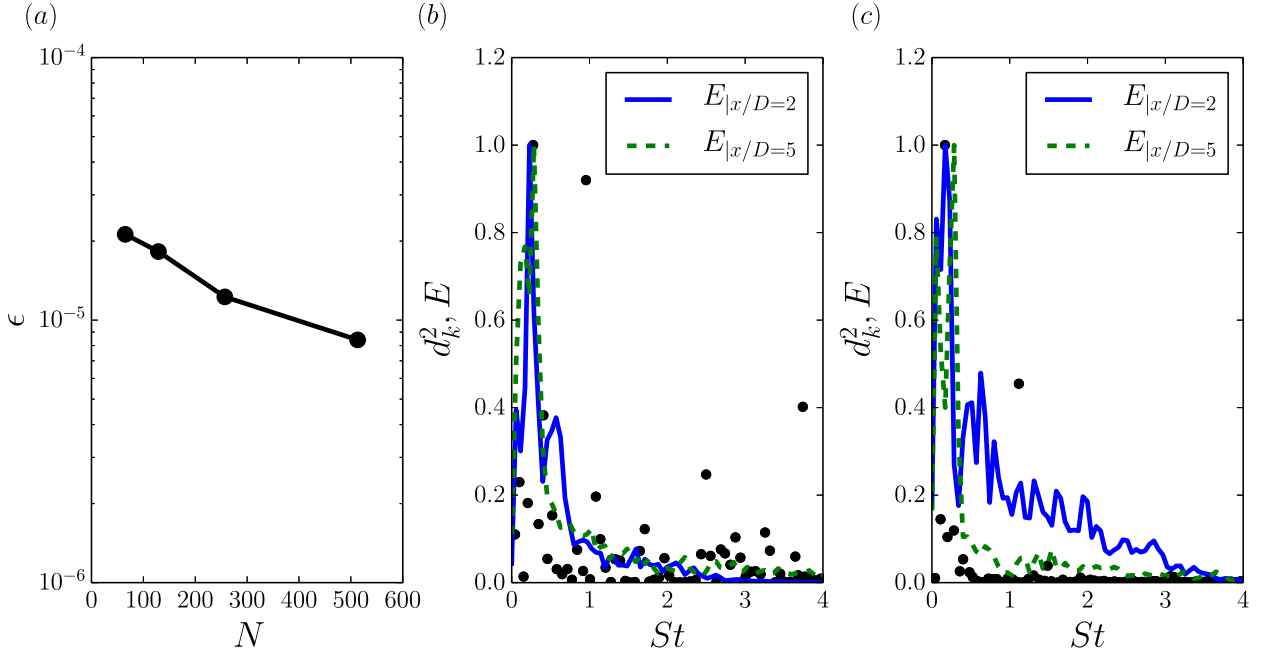


FIG. 17. Validation of dynamic mode decomposition. (a) Residuals norm ϵ of DMD modes as number of modes N increases. Dynamic mode energy spectrum d_k^2 (circle), energy spectrum at $x/D = 2$ (solid), energy spectrum at $x/D = 5$ (dashed) for (b) R2-BN and (c) R3-BN.

present in the spectral analysis with hub vortex frequency only present in the energy spectrum at $x/D = 2$ and the wake meandering present at both energy spectra shown. Moreover, the favorable comparison of the energy spectra and energy of the dynamic modes validate using the time between snapshots of $\Delta t = T/12$ and number of snapshots $N = 512$ to capture wake meandering dynamics. However, due to the location chosen for the energy spectra, the high frequencies related to the rotor frequency are not captured but are found readily in DMD. In the higher frequencies of the dynamic mode, $St > 1$, there are several peaks including the rotor frequency of $St = 2.3$. The energized modes with high frequencies including $St = 1$ relate to the rotor frequencies. Most high frequencies have a lower contribution to the energy of the flow compared to the low frequency modes like wake meandering and are related to energy modes present very close to the turbine blades.

Next, we begin analysis on the spatial modes provided by DMD of the simulations with the nacelle model for both operating conditions. We select the modes pertaining to the meandering wake and the hub vortex. Figure 18(a) shows the wake meandering dynamic mode with a $St = 0.29$ represented by the streamwise coherent velocity u_k and the two-dimensional ($x - z$) plane vector field for the simulation in Region 2. The dynamic mode shows structures of sources and sinks of the streamwise coherent velocity at $x/D > 2$ consistent instantaneous velocity of wake meandering from Fig. 11(a). The structures expand in the streamwise direction similar to wake meandering shown through the wavelength elongation due to the recovering wake. The streamwise coherent velocity from the dynamic mode corresponding to wake meandering with a frequency $St = 0.3$ in the simulation in Region 3 is shown in Fig. 18(b). Similar to the dynamic mode of the simulation in Region 2, sinks and sources in the coherent velocity appear downstream of the turbine. The wake meandering features begin to form further downstream in agreement with the mean and instantaneous flow fields of the simulation with the nacelle model in Region 3. The meandering patterns are slightly weaker and are pulled more towards the centerline than in the simulation in Region 2. Another noteworthy feature the wake meandering dynamic mode in both simulations is the prominent velocity regions around the location of the hub vortex. The velocity field in the mode shows an elongation and expansion of the hub vortex. Separate spatial dynamic modes contains more of the dynamics of the hub vortex. The strongest hub vortex mode in the simulation in Region 2 with a frequency $St = 0.73$, with an energy d_k^2 about 40% of the wake meandering energy, is shown in Fig. 18(c). There is a strong streamwise velocity near the nacelle, indicative of the meandering in the inner wake caused by the hub vortex. The streamwise velocity expands outwards towards the tip shear layers quickly in agreement with the analysis of the instantaneous wake. Downstream of the expansion towards the tip shear layers, the coherent meandering of the hub vortex is lost, but high fluctuations persists far downstream. The mode

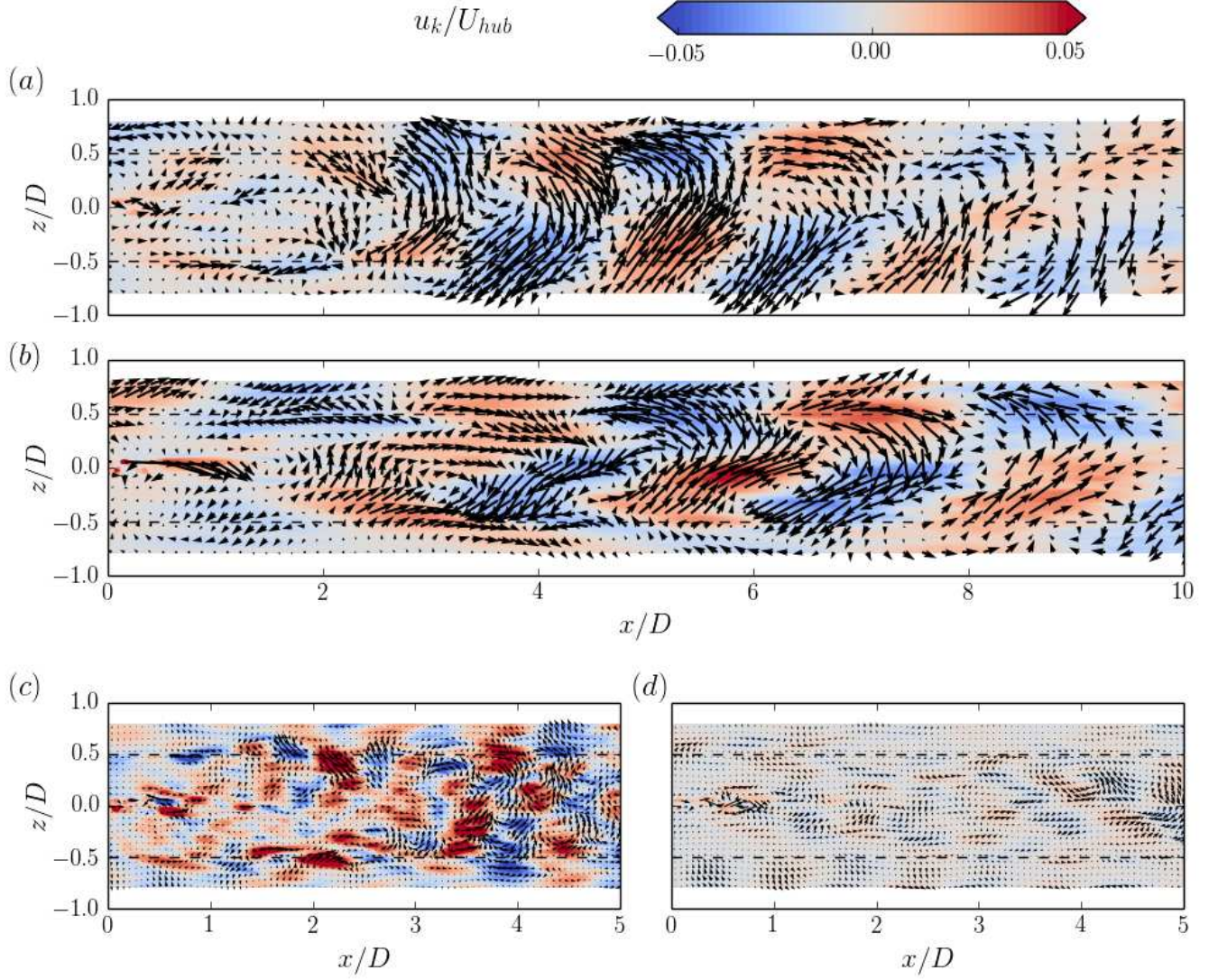


FIG. 18. Selected dynamic modes visualized by contours of the streamwise velocity and two dimensional ($x - z$) plane vector field. (a) R2-BN: $St = 0.29$, (b) R3-BN: $St = 0.3$, (c) R2-BN: $St = 0.73$, and (d) R3-BN: $St = 0.74$.

demonstrates that the hub vortex has an impact downstream as spectral analysis in Fig. 14(a) suggests. Figure 18(d) shows the streamwise coherent velocity dynamic mode of the simulation in Region 3 with a frequency of $St = 0.74$. The dynamic mode of the hub vortex is very different than the simulation of Region 2. The streamwise velocity remains in its tight spiral around the centerline with weak positive and negative regions of the streamwise coherent velocity. The Region 3 hub vortex mode is further evidence that the hub vortex does not expand quickly and interact with the tip shear layer with a similar intensity as seen in the simulation of Region 2. It is clear that operating condition affects the expansion and stability of the hub vortex.

To elucidate and characterize how certain frequencies create the dynamics in the far wake, the dynamic modes related to wake meandering and hub vortex shown in Fig. 18 are extracted to obtain a coherent velocity and used in conjunction with the meander reconstruction analysis described in the previous section V.3. Instead of using the finite temporal averaging to obtain a coherent velocity, the coherent velocity of the selected dynamic modes is used, and the velocity is used to create dynamic mode meander profiles with similarities to the meander profile statistics shown above. Two dynamic mode meandering profiles are created from selected dynamic modes: i) Summing the

wake meandering mode and hub vortex mode (h+m) and ii) Selecting only the wake meandering mode (m). The mean velocity and coherent velocity $U + u_k = U + \bar{u}$ are used to find where the velocity minima are located at each axial location downstream of the turbine just like described in the section above. The dynamic mode meander profile is obtained by low-pass spatial filtering of the velocity minima with a cutoff length scale $l_c = D/2$ which is the same filtering used for the meander profiles discussed in the previous section. Dynamic mode meander profiles are collected for each time instance using the reconstructed velocity from only selected dynamic modes.

Figure 19(a) shows an instance of both dynamic mode meander profiles and with a meander profile created using finite average filtering overlaid on the velocity $U + u_k$ from the simulation with the nacelle model in Region 2. Immediately downstream of the turbine, both dynamic mode meander profiles have an increased amplitude but a similar wavelength to the finite average filtering. In the near wake, the meander profiles created with and without using the hub vortex mode show significant difference until $x/D = 2.5$ where the profiles begin to converge. The hub vortex mode interacts with the wake meandering mode. However, the hub vortex mode has a large contribution to the meander profile after $x/D = 5$ where both profiles begin to diverge again. The dynamic meander profiles from the simulation in Region 3, shown in Fig. 19(b), are similar to each other until $x/D = 6$ where the profiles begin to diverge. This is in contrast to the Region 2 profile because in Region 3 the hub vortex mode is significantly weaker.

The average amplitude \bar{A}/D of the dynamic mode meander profiles is shown in Fig. 19(c). The statistics of the dynamic mode meander profile for Region 2 reveal that the mean amplitude is slightly higher for the (h+m) profile which includes the hub vortex compared to the (m) profile. There is not a significant difference. The hub vortex mode has a large effect on the average amplitude of the dynamic mode meander profile for simulation in Region 3. The average amplitude for the (h+m) profile is significantly higher. The average amplitude for both turbine operating regions is able to capture the trends of the wake meandering and is higher compared with the corresponding meander profile amplitude shown in Fig. 15(e). The higher amplitude in the far wake for the dynamic modes suggests that there are some higher frequency modes that smooth wake meandering. However, the wavelength statistics in Fig. 19(d) show conclusively that the two dynamic modes can fully capture the expansion and elongation of the meandering wake as the average wavelength compares well with the Fig. 15(f). The wavelength grows relatively linearly, and it suggests that the wake meandering dynamic mode is responsible because of the gradual elongation of the coherent regions in the streamwise velocity. Probability density functions of the amplitudes of the dynamic mode meander profiles at $x/D = 3$ and $x/D = 6$ are shown in Fig. 19(e) and Fig. 19(f), respectively. Noticeable is that the meander profiles that contain the hub vortex have a higher probability of larger amplitudes. While using two modes should affect the amount of energy, compared to only using the wake meandering mode, the energy and amplitude far from the turbine are higher where the hub vortex mode must have a large effect.

The above analysis shows that at a minimum two dynamic modes are needed to capture most of the fundamental features of wake meandering downstream in the wake. While the energy of the meandering wake is slightly over-predicted with the two modes, the wavelength is captured quite well. Figure 20(a) shows the ratio of the average amplitude of the dynamic mode meander profile to the filtered meander profile of the complete flow field at $x/D = 8$ as the number of dynamic modes, arranged by frequency in ascending order, are included in the flow field. It shows conclusively that the amplitude of the meandering profile using dynamic mode decomposition converges to the meander profile using the temporal filtering with just a few of the low frequency modes for either operating condition. For the simulation in Region 2 there are five dynamic modes in the frequency range of $0 < St \leq 0.29$, and four dynamic modes included from $0.29 < St \leq 0.73$. Similarly for Region 3, there are four dynamic modes included in both the frequency range of $0 < St \leq 0.3$ and $0.3 < St \leq 0.74$. Less than 2% of the dynamic modes, all from the low frequency range, are needed to capture most of the energy in the fundamental spanwise oscillation of wake meandering. Both profiles from each operating condition increase monotonically from $St = 0$ to $St = 0.74$, the hub vortex frequency. After, the ratio slowly converges to unity. This is a further indication that the low frequency meandering is captured using a few modes, namely, the modes corresponding to the wake meandering and hub vortex frequency. Figure 20(b) similarly shows the ratio of the average meander profile wavelength of the dynamic mode decomposition to temporal filtering meandering profile at $x/D = 8$. The wavelength ratio peaks for both operating conditions at $St = 0.34$, near the wake meandering frequency, but when the hub vortex frequency is included, for a total of nine and eight dynamic modes for Region 2 and 3, respectively, the ratio trends towards unity showing that few modes are necessary, most especially the wake meandering and hub vortex dynamic modes, for prescribing the dynamic motions of the wake.

VI. DISCUSSION AND CONCLUSIONS

Wind tunnel experiments and numerical experiments using large-eddy simulations are carried out to investigate the flow past a model wind turbine with a rotor diameter of 1.1 meters operating in Region 2 and Region 3. The incoming turbulent flow is generated by spires at the inlet of wind tunnel in both the experiments and simulations. The statistics of the wake behind the wind turbine predicted by the simulations are in good agreement with measurements.

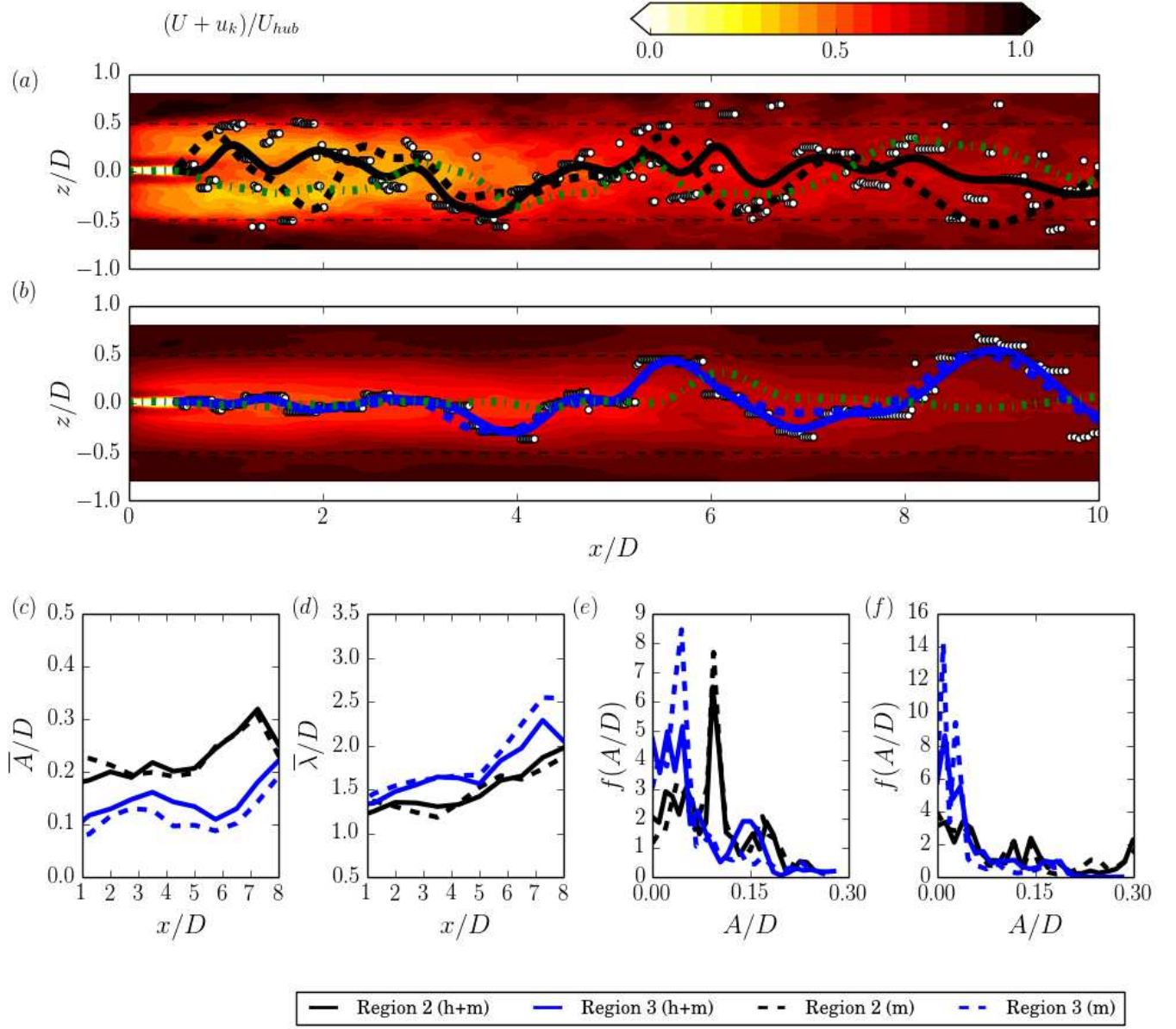


FIG. 19. Dynamic mode meander profiles created from hub vortex and wake meandering mode (h+m), dynamic mode meander profile from wake meandering mode (m) and meander profile from complete flow field overlaid on contours and velocity minima (white dots) of the sum of the average velocity and selected hub vortex and wake meandering modes, $U + u_k$, non-dimensionalized by the hub velocity U_{hub} for (a) R2-BN and (b) R3-BN. For reference, the corresponding temporal averaged wake meander profile is shown (dashed-dotted line). Characteristics of dynamic mode meander profiles (c) amplitude, \bar{A} , and (d) wavelength $\bar{\lambda}$ with respect to distance from rotor plane. Probability density function of amplitude, A/D , at (e) $x/D = 3$ and (f) $x/D = 6$.

Simulations with and without a nacelle model are carried out to systematically study its effect on the hub vortex and meandering motions at far wake locations. While the simulations without a nacelle model accurately predict the mean velocity profiles in the far wake, they fail to capture the wake just behind the nacelle, instead predicting a jet and significantly different distributions of turbulence intensity close to the turbine along the centerline. Specifically, the hub vortex along the centerline remains a columnar jet for the simulations without a nacelle model. Wake meandering with its downwind locations correlate well with the high turbulence intensity region for both simulations with and without a nacelle model. However, the simulations without a nacelle model predict lower turbulence intensity at far wake locations, and the location for maximum turbulence intensity is further downwind. Significant influence of turbine operating conditions on far wake turbulence intensity and wake meandering is observed: large amplitude wake

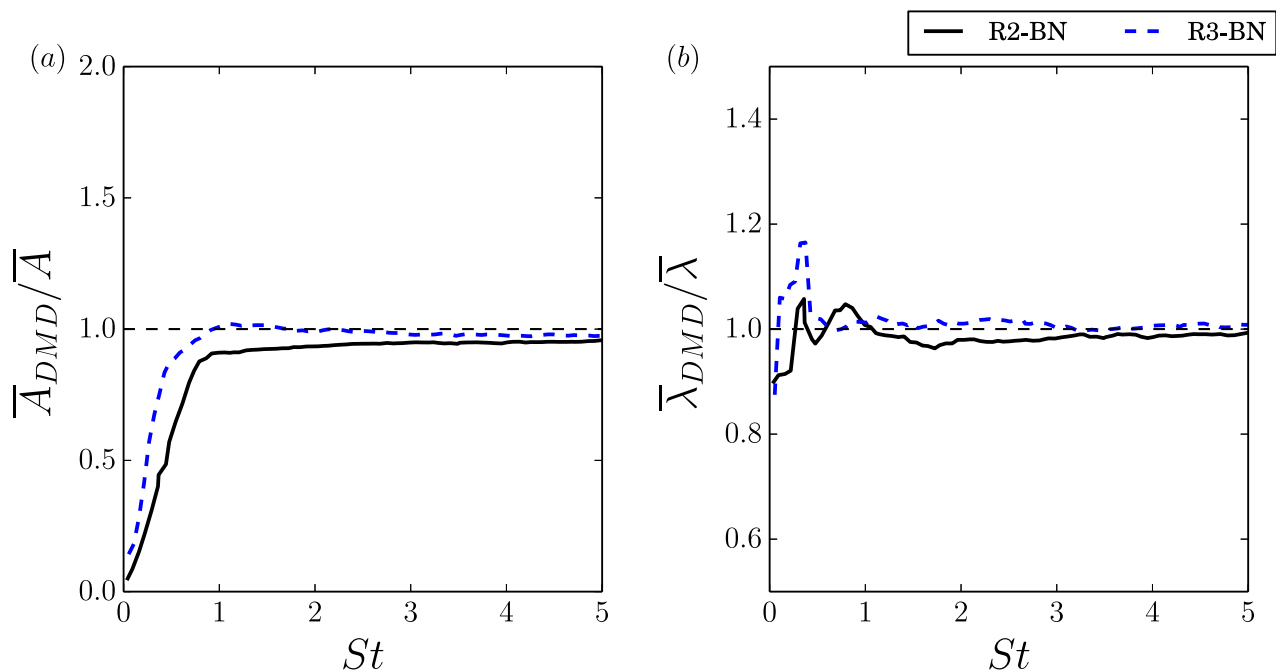


FIG. 20. Ratio of (a) the averaged amplitude and (b) the averaged wavelength of the dynamic mode meander profiles to those from the complete flow field as the number of employed frequency modes in ascending order are increased at $x/D = 8$.

meandering happens further downwind and the length of the region with high turbulence intensity is significantly longer for the Region 3 operating condition.

To further investigate the characteristics of wake meandering for different operating conditions and the effects of the nacelle, the instantaneous large-scale coherent wake meander profiles are constructed using the finite time averaging technique developed by Howard *et al.* [26] and Foti *et al.* [22]. We show that the amplitude of wake meandering is less for the simulations without a nacelle model for both operating conditions. Also, the amplitude is lower in the turbine operating in Region 3 in comparison to Region 2. However, the wavelength and growth rate of wavelength for wake meandering are similar at different downwind locations regardless of nacelle modeling or turbine operating conditions.

The wake meandering frequency is associated with a $St \sim 0.3$ in many different studies (Okulov *et al.* [3], Medici and Alfredsson [24], Chamorro *et al.* [25]), while the hub vortex is measured to have a frequency with $St \sim 0.7$ in Iungo *et al.* [20], Howard *et al.* [26] and Foti *et al.* [22]. For the present turbine, frequencies in those ranges are found for both turbine operating conditions. The spectral analysis reveals that the presence of these frequencies correlates with the locations where the coherent motions of wake meandering and the hub vortex are most prevalent. Dynamic mode decomposition of the flow allows us to extract and isolate the select modes related to both the wake meandering frequency and the hub vortex frequency. The wake meandering dynamic mode consists of a large coherent oscillatory motions in the far wake. The hub vortex dynamic mode, while strongest around the nacelle, persists far downstream, especially in Region 2 where the hub vortex is more unstable. Two meandering profiles are created, one using only the wake meandering mode and another using both the wake meandering and hub vortex modes. It is observed that the amplitude of the meandering profile using both modes is higher than that only using the wake meandering mode, especially for downstream locations.

From the evidence provided through our analyses, our work has further confirmed the importance of the nacelle on wake meandering at the far wake for a 1.1 meters diameter wind turbine under different operating conditions in addition to previous works for a 0.5 meters diameter hydrokinetic turbine [4] and a 0.13 meters model wind turbine [22]. In the future work, we will look at the effects of the nacelle on the wake meandering dynamics in utility-scale wind farms and explore how the investigated wake meandering statistics can be employed in reduced-order models.

ACKNOWLEDGMENTS

This work was supported by U.S. Department of Energy (DE-EE0002980, DE-EE0005482 and DE-AC04-94AL85000), Xcel Energy through the Renewable Development Fund (grant RD4-13), and Sandia National Laboratories. Computational resources were provided by Sandia National Laboratories and the University of Minnesota Supercomputing Institute. Sandia National Laboratories is a multimission laboratory managed and operated by National Technology and Engineering Solutions of Sandia, LLC, a wholly owned subsidiary of Honeywell International, Inc., for the U.S. Department of Energy's National Nuclear Security Administration under contract DE-NA0003525.

-
- [1] Rebecca Jane Barthelmie, K Hansen, Sten Tronæs Frandsen, Ole Rathmann, JG Schepers, W Schlez, J Phillips, K Rados, A Zervos, ES Politis, *et al.*, “Modelling and measuring flow and wind turbine wakes in large wind farms offshore,” *Wind Energy* **12**, 431–444 (2009).
 - [2] Said El-Asha, Lu Zhan, and Giacomo Valerio Iungo, “Quantification of power losses due to wind turbine wake interactions through scada, meteorological and wind lidar data,” *Wind Energy* **20**, 1823–1839 (2017).
 - [3] Valery L Okulov, Igor V Naumov, Robert F Mikkelsen, Ivan K Kabardin, and Jens N Sørensen, “A regular strouhal number for large-scale instability in the far wake of a rotor,” *Journal of Fluid Mechanics* **747**, 369–380 (2014).
 - [4] Seokkoo Kang, Xiaolei Yang, and Fotis Sotiropoulos, “On the onset of wake meandering for an axial flow turbine in a turbulent open channel flow,” *Journal of Fluid Mechanics* **744**, 376–403 (2014).
 - [5] Daniel Foti, Xiaolei Yang, and Fotis Sotiropoulos, “Similarity of wake meandering for different wind turbine designs for different scales,” *Journal of Fluid Mechanics* **842**, 5–25 (2018).
 - [6] Gunner C Larsen, Helge Aa Madsen, Kenneth Thomsen, and Torben J Larsen, “Wake meandering: a pragmatic approach,” *Wind energy* **11**, 377–395 (2008).
 - [7] Xiaolei Yang, Seokkoo Kang, and Fotis Sotiropoulos, “Computational study and modeling of turbine spacing effects in infinite aligned wind farms,” *Physics of Fluids* **24**, 115107 (2012).
 - [8] NE Joukowski, “Vortex theory of a rowing screw,” *Trudy Otdeleniya Fizicheskikh Nauk Obshchestva Lubitelei Estestvoznaniya* **16** (1912).
 - [9] Leonardo P Chamorro and Fernando Porté-Agel, “A wind-tunnel investigation of wind-turbine wakes: boundary-layer turbulence effects,” *Boundary-layer meteorology* **132**, 129–149 (2009).
 - [10] Hui Hu, Zifeng Yang, and Partha Sarkar, “Dynamic wind loads and wake characteristics of a wind turbine model in an atmospheric boundary layer wind,” *Experiments in fluids* **52**, 1277–1294 (2012).
 - [11] Michael Sherry, András Nemes, David Lo Jacono, Hugh M Blackburn, and John Sheridan, “The interaction of helical tip and root vortices in a wind turbine wake,” *Physics of Fluids* **25**, 117102 (2013).
 - [12] Jiarong Hong, Mostafa Toloui, Leonardo P Chamorro, Michele Guala, Kevin Howard, Sean Riley, James Tucker, and Fotis Sotiropoulos, “Natural snowfall reveals large-scale flow structures in the wake of a 2.5-mw wind turbine,” *Nature communications* **5** (2014).
 - [13] Stefan Ivanell, Jens N Sørensen, Robert Mikkelsen, and Dan Henningson, “Analysis of numerically generated wake structures,” *Wind Energy* **12**, 63–80 (2009).
 - [14] Stefan Ivanell, Robert Mikkelsen, Jens N Sørensen, and Dan Henningson, “Stability analysis of the tip vortices of a wind turbine,” *Wind Energy* **13**, 705–715 (2010).
 - [15] Niels Troldborg, Jens N Sørensen, and Robert Mikkelsen, “Actuator line simulation of wake of wind turbine operating in turbulent inflow,” in *Journal of Physics: Conference Series*, Vol. 75 (IOP Publishing, 2007) p. 012063.
 - [16] M Felli, R Camussi, and F Di Felice, “Mechanisms of evolution of the propeller wake in the transition and far fields,” *Journal of Fluid Mechanics* **682**, 5–53 (2011).
 - [17] Sasan Sarmast, Reza Dadfar, Robert F Mikkelsen, Philipp Schlatter, Stefan Ivanell, Jens N Sørensen, and Dan S Henningson, “Mutual inductance instability of the tip vortices behind a wind turbine,” *Journal of Fluid Mechanics* **755**, 705–731 (2014).
 - [18] Xiaolei Yang, Jiarong Hong, Matthew Barone, and Fotis Sotiropoulos, “Coherent dynamics in the rotor tip shear layer of utility-scale wind turbines,” *Journal of Fluid Mechanics* **804**, 90–115 (2016).
 - [19] VL Okulov and Jens Nørkær Sørensen, “Stability of helical tip vortices in a rotor far wake,” *Journal of Fluid Mechanics* **576**, 1–25 (2007).
 - [20] Giacomo Valerio Iungo, Francesco Viola, Simone Camarri, Fernando Porté-Agel, and François Gallaire, “Linear stability analysis of wind turbine wakes performed on wind tunnel measurements,” *Journal of Fluid Mechanics* **737**, 499–526 (2013).
 - [21] F Viola, GV Iungo, S Camarri, F Porté-Agel, and F Gallaire, “Prediction of the hub vortex instability in a wind turbine wake: stability analysis with eddy-viscosity models calibrated on wind tunnel data,” *Journal of Fluid Mechanics* **750**, R1 (2014).
 - [22] Daniel Foti, Xiaolei Yang, Michele Guala, and Fotis Sotiropoulos, “Wake meandering statistics of a model wind turbine: Insights gained by large eddy simulations,” *Physical Review Fluids* **1**, 044407 (2016).
 - [23] Davide Medici and PH Alfredsson, “Measurements on a wind turbine wake: 3d effects and bluff body vortex shedding,” *Wind Energy* **9**, 219–236 (2006).

- [24] D Medici and P Henrik Alfredsson, “Measurements behind model wind turbines: further evidence of wake meandering,” *Wind Energy* **11**, 211–217 (2008).
- [25] LP Chamorro, C Hill, S Morton, C Ellis, REA Arndt, and F Sotiropoulos, “On the interaction between a turbulent open channel flow and an axial-flow turbine,” *Journal of Fluid Mechanics* **716**, 658–670 (2013).
- [26] Kevin B Howard, Arvind Singh, Fotis Sotiropoulos, and Michele Guala, “On the statistics of wind turbine wake meandering: An experimental investigation,” *Physics of Fluids* **27**, 075103 (2015).
- [27] Per-Åge Krogstad and Pål Egil Eriksen, “blind test calculations of the performance and wake development for a model wind turbine,” *Renewable energy* **50**, 325–333 (2013).
- [28] PØel Egil Eriksen and Per-Åge Krogstad, “Experimental results for the nowitech/norcowe blindtest,” *Energy Procedia* **24**, 378–384 (2012).
- [29] MS Adaramola and P-Å Krogstad, “Experimental investigation of wake effects on wind turbine performance,” *Renewable Energy* **36**, 2078–2086 (2011).
- [30] Fabio Pierella, Per-Åge Krogstad, and Lars Sætran, “Blind test 2 calculations for two in-line model wind turbines where the downstream turbine operates at various rotational speeds,” *Renewable Energy* **70**, 62–77 (2014).
- [31] H Snel, JG Schepers, and B Montgomerie, “The mexico project (model experiments in controlled conditions): The database and first results of data processing and interpretation,” in *Journal of Physics: Conference Series*, Vol. 75 (IOP Publishing, 2007) p. 012014.
- [32] JG Schepers, K Boorsma, and X Munduate, “Final results from mexnext-i: Analysis of detailed aerodynamic measurements on a 4.5 m diameter rotor placed in the large german dutch wind tunnel dnw,” in *Journal of Physics: Conference Series*, Vol. 555 (IOP Publishing, 2014) p. 012089.
- [33] Hermann Glauert, “Airplane propellers,” in *Aerodynamic theory* (Springer, 1935) pp. 169–360.
- [34] Marc Calaf, Charles Meneveau, and Johan Meyers, “Large eddy simulation study of fully developed wind-turbine array boundary layers,” *Physics of Fluids* **22**, 015110 (2010).
- [35] Fernando Porté-Agel, Yu-Ting Wu, Hao Lu, and Robert J Conzemius, “Large-eddy simulation of atmospheric boundary layer flow through wind turbines and wind farms,” *Journal of Wind Engineering and Industrial Aerodynamics* **99**, 154–168 (2011).
- [36] Jens Nørkær Sørensen and Wen Zhong Shen, “Numerical modeling of wind turbine wakes,” *Journal of Fluids Engineering* **124**, 393–399 (2002).
- [37] Xiaolei Yang, Fotis Sotiropoulos, Robert J Conzemius, John N Wachtler, and Mike B Strong, “Large-eddy simulation of turbulent flow past wind turbines/farms: the virtual wind simulator (vwis),” *Wind Energy* **18**, 2025–2045 (2015).
- [38] Wen Zhong Shen, Jens Nørkær Sørensen, and Jianhui Zhang, “Actuator surface model for wind turbine flow computations,” in *2007 European Wind Energy Conference & Exhibition* (2007).
- [39] Guillaume España, Sandrine Aubrun, Stéphane Loyer, and Philippe Devinant, “Spatial study of the wake meandering using modelled wind turbines in a wind tunnel,” *Wind Energy* **14**, 923–937 (2011).
- [40] Hamid Sarlak, C Meneveau, and Jens Nørkær Sørensen, “Role of subgrid-scale modeling in large eddy simulation of wind turbine wake interactions,” *Renewable Energy* **77**, 386–399 (2015).
- [41] Anshul Mittal, Kidambi Sreenivas, Lafayette K Taylor, Levi Hereth, and Christopher B Hilbert, “Blade-resolved simulations of a model wind turbine: effect of temporal convergence,” *Wind Energy* **19**, 1761–1783 (2016).
- [42] Ryan Ashton, Francesco Viola, Simone Camarri, Francois Gallaire, and Giacomo Valerio Iungo, “Hub vortex instability within wind turbine wakes: Effects of wind turbulence, loading conditions, and blade aerodynamics,” *Physical Review Fluids* **1**, 073603 (2016).
- [43] Christian Santoni, Kenneth Carrasquillo, Isnardo Arenas-Navarro, and Stefano Leonardi, “Effect of tower and nacelle on the flow past a wind turbine,” *Wind Energy* **20**, 1927–1939 (2017).
- [44] Richard JAM Stevens, Luis A Martínez-Tossas, and Charles Meneveau, “Comparison of wind farm large eddy simulations using actuator disk and actuator line models with wind tunnel experiments,” *Renewable Energy* **116**, 470–478 (2018).
- [45] Xiaolei Yang and Fotis Sotiropoulos, “A new class of actuator surface models for wind turbines,” *Wind Energy* , 1–18 (2018).
- [46] Mahdi Abkar and Fernando Porté-Agel, “Influence of atmospheric stability on wind-turbine wakes: A large-eddy simulation study,” *Physics of Fluids* **27**, 035104 (2015).
- [47] Lucy Y Pao and Kathryn E Johnson, “A tutorial on the dynamics and control of wind turbines and wind farms,” in *2009 American Control Conference* (IEEE, 2009) pp. 2076–2089.
- [48] Peter J Schmid, “Dynamic mode decomposition of numerical and experimental data,” *Journal of Fluid Mechanics* **656**, 5–28 (2010).
- [49] Filippo Campagnolo, *Wind tunnel testing of scaled wind turbine models: aerodynamics and beyond*, Ph.D. thesis, Politecnico Di Milano (2013).
- [50] Filippo Campagnolo, Vlaho Petrović, Johannes Schreiber, Emmanouil M Nanos, Alessandro Croce, and Carlo L Bottasso, “Wind tunnel testing of a closed-loop wake deflection controller for wind farm power maximization,” in *Journal of Physics: Conference Series*, Vol. 753 (IOP Publishing, 2016) p. 032006.
- [51] C.A. Lyon, A.P. Broeren, P. Gigure, A. Gopalarathnam, and M.S. Selig, *Summary of Low-Speed Airfoil Data*, Vol. 3 (SoarTech Publications, 1998).
- [52] T. Burton, D. Sharpe, N. Jenkins, and E. Bossanyi, *Wind Energy Handbook* (Wiley, 2001).
- [53] C.L. Bottasso, S. Cacciola, and X. Iriarte, “Calibration of wind turbine lifting line models from rotor loads,” *Journal of Wind Engineering and Industrial Aerodynamics* **124**, 29–45 (2014).
- [54] E. Bossanyi, “The design of closed loop controllers for wind turbines,” *Wind Energy* **3**, 149–163 (2000).

- [55] Liang Ge and Fotis Sotiropoulos, “A numerical method for solving the 3d unsteady incompressible navier–stokes equations in curvilinear domains with complex immersed boundaries,” *Journal of Computational Physics* **225**, 1782–1809 (2007).
- [56] Anvar Gilmanov and Fotis Sotiropoulos, “A hybrid cartesian/immersed boundary method for simulating flows with 3d, geometrically complex, moving bodies,” *Journal of Computational Physics* **207**, 457–492 (2005).
- [57] Joseph Smagorinsky, “General circulation experiments with the primitive equations: I. the basic experiment*,” *Monthly weather review* **91**, 99–164 (1963).
- [58] Massimo Germano, Ugo Piomelli, Parviz Moin, and William H Cabot, “A dynamic subgrid-scale eddy viscosity model,” *Physics of Fluids A: Fluid Dynamics (1989-1993)* **3**, 1760–1765 (1991).
- [59] Vincenzo Armenio and Ugo Piomelli, “A lagrangian mixed subgrid-scale model in generalized coordinates,” *Flow, Turbulence and Combustion* **65**, 51–81 (2000).
- [60] Mark Drela, “Xfoil: An analysis and design system for low reynolds number airfoils,” in *Low Reynolds Number Aerodynamics* (Springer, 1989) pp. 1–12.
- [61] Xiaolei Yang, Xing Zhang, Zhilin Li, and Guo-Wei He, “A smoothing technique for discrete delta functions with application to immersed boundary method in moving boundary simulations,” *Journal of Computational Physics* **228**, 7821–7836 (2009).
- [62] Zhaohui Du and Michael S Selig, “A 3-d stall-delay model for horizontal axis wind turbine performance prediction,” in *1998 ASME Wind Energy Symposium*, Vol. 21 (1998).
- [63] Wen Zhong Shen, Robert Mikkelsen, Jens Nørkær Sørensen, and Christian Bak, “Tip loss corrections for wind turbine computations,” *Wind Energy* **8**, 457–475 (2005).
- [64] Markus Uhlmann, “An immersed boundary method with direct forcing for the simulation of particulate flows,” *Journal of Computational Physics* **209**, 448–476 (2005).
- [65] Herrmann Schlichting and Klaus Gersten, *Boundary-Layer Theory* (Springer Science & Business Media, 2003).
- [66] Daniel Foti, Xiaolei Yang, Filippo Campagnolo, David Maniaci, and Fotis Sotiropoulos, “On the use of spires for generating inflow conditions with energetic coherent structures in large eddy simulation,” *Journal of Turbulence* **18**, 611–633 (2017).
- [67] Seokkoo Kang and Fotis Sotiropoulos, “Numerical modeling of 3d turbulent free surface flow in natural waterways,” *Advances in Water Resources* **40**, 23–36 (2012).
- [68] Leonardo P Chamorro, REA Arndt, and F Sotiropoulos, “Reynolds number dependence of turbulence statistics in the wake of wind turbines,” *Wind Energy* **15**, 733–742 (2012).
- [69] Niels Troldborg, Jens N Sørensen, and Robert Mikkelsen, “Numerical simulations of wake characteristics of a wind turbine in uniform inflow,” *Wind Energy* **13**, 86–99 (2010).
- [70] Ángel Jiménez, Antonio Crespo, and Emilio Migoya, “Application of a les technique to characterize the wake deflection of a wind turbine in yaw,” *Wind energy* **13**, 559–572 (2010).
- [71] Michael F Howland, Juliaan Bossuyt, Luis A Martínez-Tossas, Johan Meyers, and Charles Meneveau, “Wake structure in actuator disk models of wind turbines in yaw under uniform inflow conditions,” *Journal of Renewable and Sustainable Energy* **8**, 043301 (2016).
- [72] Juan-José Trujillo, Ferhat Bingöl, Gunner C Larsen, Jakob Mann, and Martin Kühn, “Light detection and ranging measurements of wake dynamics. part ii: two-dimensional scanning,” *Wind Energy* **14**, 61–75 (2011).
- [73] Paul A Fleming, Pieter MO Gebraad, Sang Lee, Jan-Willem van Wingerden, Kathryn Johnson, Matt Churchfield, John Michalakes, Philippe Spalart, and Patrick Moriarty, “Evaluating techniques for redirecting turbine wakes using sowfa,” *Renewable Energy* **70**, 211–218 (2014).
- [74] A Chrisohoides and F Sotiropoulos, “Experimental visualization of lagrangian coherent structures in aperiodic flows,” *Physics of Fluids* **15**, L25–L28 (2003).
- [75] A Hussain, “Coherent structures and turbulence,” *Journal of Fluid Mechanics* **173**, 303–356 (1986).
- [76] Clarence W Rowley, Igor Mezić, Shervin Bagheri, Philipp Schlatter, and Dan S Henningson, “Spectral analysis of nonlinear flows,” *Journal of Fluid Mechanics* **641**, 115–127 (2009).